



# 1 Satellite Observations of Smoke-Cloud- 2 Radiation Interactions Over the Amazon 3 Rainforest

4 **Ross Herbert<sup>1</sup> and Philip Stier<sup>1</sup>**

5 <sup>1</sup> Atmospheric, Oceanic, and Planetary Physics, Department of Physics, University of  
6 Oxford, Oxford, OX1 3PU, United Kingdom

7 *Correspondence to:* Ross Herbert (ross.herbert@physics.ox.ac.uk)

## 8 **Abstract**

9 The Amazon rainforest routinely experiences intense and long-lived biomass burning events that  
10 result in smoke plumes that cover vast regions. The spatial and temporal extent of the plumes, and the  
11 complex pathways through which they interact with the atmosphere, has proved challenging to measure  
12 and gain a representative understanding of smoke impacts on the Amazonian atmosphere. In this study  
13 we use multiple collocated satellite sensors onboard AQUA and TERRA platforms to study the  
14 underlying smoke-cloud-radiation interactions during the diurnal cycle. An 18-year timeseries for both  
15 morning and afternoon overpasses is constructed providing collocated measurements of aerosol optical  
16 depth (column integrated aerosol extinction, AOD), cloud properties, top-of-atmosphere radiative  
17 fluxes, precipitation, and column water-vapour content from independent sources.  
18

19 The long-term timeseries reduces the impact of interannual variability and provides robust evidence  
20 that smoke significantly modifies the Amazonian atmosphere. Low loadings of smoke ( $AOD \leq 0.4$ )  
21 enhance convective activity, cloudiness and precipitation, but higher loadings ( $AOD > 0.4$ ) strongly  
22 suppress afternoon convection and promote low-level cloud occurrence. Accumulated precipitation  
23 increases with convective activity but remains elevated under high smoke loadings suggesting fewer  
24 but more intense convective cells. Contrasting morning and afternoon cloud responses to smoke are  
25 observed, in-line with recent simulations. Observations of top-of-atmosphere radiative fluxes support  
26 the findings, and show that the response of low-level cloud properties and cirrus coverage to smoke  
27 results in a pronounced and consistent increase in top-of-atmosphere outgoing radiation (cooling) of up  
28 to  $50 \text{ Wm}^{-2}$  for an AOD perturbation of +1.0.  
29

30 The results demonstrate that smoke strongly modifies the atmosphere over the Amazon via  
31 widespread changes to the cloud-field properties. Rapid adjustments work alongside instantaneous  
32 radiative effects to drive a stronger cooling effect from smoke than previously thought, whilst  
33 contrasting morning / afternoon responses of liquid and ice water paths highlight a potential method for  
34 constraining aerosol impacts on climate. Increased drought susceptibility, land-use change, and  
35 deforestation will have important and widespread impacts to the region over the coming decades. Based  
36 on this analysis, we anticipate further increases in anthropogenic fire activity to be associated with an  
37 overall reduction in regional precipitation, and a negative forcing (cooling) on the Earth's energy  
38 budget.

## 39 **1. Introduction**

40 Anthropogenic aerosols and their role in the earth system remain a key uncertainty in quantifying the  
41 impact of historic and future anthropogenic activity on the global climate (Forster et al., 2021). Aerosols  
42 interact with the atmosphere via modifying fluxes of solar and terrestrial radiation (referred to as



43 aerosol-radiation interactions, ARI) and by influencing the properties of clouds (referred to as aerosol-  
44 cloud interactions, ACI), and therefore have the potential to significantly alter surface fluxes, cloud  
45 properties, precipitation, and the energy budget of the atmosphere.

46

47 Biomass burning produces smoke aerosol particles that efficiently absorb shortwave radiation and  
48 strongly perturb the atmosphere via both ARI and ACI processes. Smoke instantaneously reduces  
49 shortwave radiation reaching the surface and produces localised warming of the smoke layer via the  
50 ARI pathway. Rapid adjustments of the environment due to ARI can result in reduced surface fluxes  
51 and suppressed convection (Zhang et al., 2008b; Liu et al., 2020; Martins et al., 2009), with the localised  
52 warming driving cloud evaporation or deepening depending on the cloud type and relative altitude of  
53 the smoke (Koch and Del Genio, 2010; Herbert et al., 2020). Via the ACI pathway aerosol particles can  
54 act as cloud condensation nuclei (CCN) or ice nuclei (IN) and instantaneously modify the number  
55 concentration of cloud droplets or ice particles in a given cloud thus changing the cloud albedo. Rapid  
56 adjustments associated with ACI include changes to precipitation efficiency and cloud evolution (Wu  
57 et al., 2011; Liu et al., 2020; Thornhill et al., 2018; Marinescu et al., 2021; Zaveri et al., 2022). The  
58 influence that a smoke particle has on a cloud and its environment is dependent on its physiochemical  
59 properties, which determine its optical properties and ability to act as a CCN or IN. These properties  
60 are dependent on the type of fuel (McClure et al., 2020; Petters et al., 2009), the combustion efficiency  
61 (Liu et al., 2014), and may also change with time through aging processes and interaction with other  
62 species (Vakkari et al., 2014; Zhang et al., 2008a). This, combined with the myriad of pathways through  
63 which smoke can impact the environment, and the spatial and temporal extent of the smoke plumes, has  
64 proven a challenge to understand at a process level and represent in atmospheric models. As a result,  
65 there remains considerable uncertainty in our understanding of smoke impacts to climate on a global  
66 scale (Forster et al., 2021; Bond et al., 2013), which will become increasingly important in the future  
67 as drought conditions become more prevalent (Stocker et al., 2013) and anthropogenic deforestation  
68 continues (de Oliveira et al., 2020).

69

70 The Amazon rainforest in South America is one of the world's largest sources of biomass burning  
71 aerosol (van der Werf et al., 2017), with peak emissions observed during the annual dry season (August  
72 to October) driven almost exclusively by agricultural activities and anthropogenic activity (Libonati et  
73 al., 2021). The associated smoke plumes can extend high into the troposphere (Holanda et al., 2020)  
74 and cover vast regions, with sustained high atmospheric loadings of smoke often observed for days to  
75 weeks. Observational studies have demonstrated the ability for smoke to strongly influence the Amazon  
76 atmosphere during the dry season via changes to the initiation and efficiency of precipitation processes  
77 in deep convective clouds (Andreae et al., 2004; Gonçalves et al., 2015; Camponogara et al., 2014;  
78 Bevan et al., 2008; Braga et al., 2017; Wendisch et al., 2016). These impacts are largely attributed to  
79 the suppression of convection or enhanced cloud droplet number concentrations, though the overall  
80 response of cumulative precipitation remains uncertain.

81

82 The widespread and long-lived nature of the smoke perturbations present a challenge to make the  
83 necessary in-situ measurements that capture the overall impact of the smoke on the atmosphere.  
84 Regional modelling studies with sufficient complexity to reproduce the convective nature of the  
85 Amazon atmosphere have been used to quantify the widespread smoke-cloud-radiation interactions. A  
86 consistent result is widespread suppression of convection underneath smoke plumes due to the cooler  
87 surface and elevated heating stabilising the boundary layer, and a corresponding reduction in cumulative  
88 precipitation (Martins et al., 2009; Zhang et al., 2009; Wu et al., 2011; Liu et al., 2020; Herbert et al.,  
89 2021). There is less agreement on the change to the widespread cloud field properties such as cloud  
90 fraction (CF), liquid water path (LWP), and ice water path (IWP), potentially due to the complexity of  
91 sufficiently representing ACI and ARI processes in these models (Marinescu et al., 2021; White et al.,  
92 2017). In a recent study Herbert et al. (2021) performed week-long simulations of smoke-cloud-  
93 radiation interactions over the Amazon at convection-permitting resolution. The authors reported



94 considerable diurnal variation in the cloud response with enhanced cloudiness overnight and reduced  
95 cloudiness in the afternoon; this occurred alongside a gradual increase in the IWP across the domain  
96 that strongly dictated the overall positive effective radiative forcing (ERF) due to the smoke. The  
97 response in IWP was in contrast to a similar study by Liu et al. (2020) who reported only weakly  
98 increasing IWP across the model domain, with changes in the liquid cloud fraction dictating the overall  
99 negative ERF. The contrasting results have important implications for the ERF of smoke, however,  
100 without robust observational information it is difficult to establish whether these model-based  
101 conclusions are valid.

102

103 One means of gathering this information is using space-borne remote observations that are able to  
104 provide widespread and routine coverage. Koren et al. (2004) used retrievals from the Moderate  
105 Resolution Imaging Spectroradiometer (MODIS) instrument onboard the AQUA satellite to examine  
106 cloud-smoke relationships during the 2002 dry season; the authors found that the low-cloud fraction  
107 was strongly suppressed as the smoke optical depth increased. Yu et al. (2007) similarly used MODIS-  
108 AQUA retrievals to examine widespread smoke-cloud interactions for the 2002 and 2003 dry seasons  
109 and found pronounced variability in the smoke-cloud relationships between the years studied, and  
110 considerable sensitivity to the cloud properties (e.g., LWP) in both years. This study supported the  
111 results from Koren et al. (2004), but also demonstrated important interannual variability, suggesting a  
112 longer timeseries is required to quantify and understand the underlying processes through which the  
113 smoke perturbs the widespread environment. Koren et al. (2008) used MODIS-AQUA retrievals of  
114 cloud fraction and cloud top height during the dry seasons of 2005 to 2007 to propose that the response  
115 of clouds to smoke is nonlinear: at low loadings of smoke clouds are invigorated, but at higher loadings  
116 the clouds are suppressed. These results were supported by a simplified theoretical model that  
117 additionally suggested the invigoration was driven by ACI processes, whereas the suppression was  
118 driven by ARI processes. These widespread remote observations provide valuable insight but there are  
119 several areas that can be improved upon: 1) Interannual variability – the response of the atmosphere to  
120 smoke may be different from one year to the next, which may mask the underlying smoke-cloud-  
121 radiation processes and overall impact of the smoke. 2) Diurnal cycle – modelling studies suggest  
122 important diurnal responses to the cloud and precipitation (Liu et al., 2020; Herbert et al., 2021), yet  
123 previous remote observations over the Amazon have only observed a very small window of time  
124 coinciding with the AQUA satellite overpass time (~1330 local solar time; LST). 3) Radiative effect –  
125 it is understood that smoke may have important impacts to deep convective clouds and their optical  
126 properties, yet previous studies have estimated radiative effects using offline radiative transfer models,  
127 which may not be representative of the true radiative effect

128

129 In this study we build upon previous efforts to quantitatively understand aerosol-cloud-radiative  
130 interactions by focusing on smoke impacts to the Amazonian atmosphere during the dry season. This  
131 region provides a unique opportunity to study the interactions between long-lived, substantial aerosol  
132 loadings and deep convective clouds over a widespread region. We use 18 years of satellite observations  
133 to produce a 1-degree gridded climatology of smoke-cloud-radiation effects over the Amazon during  
134 the biomass burning season. The long timeseries allows us to work towards removing or reducing the  
135 interannual variability, and provides the means to robustly explore more of the parameter space. We  
136 explore the diurnal cycle of the responses to smoke by combining and contrasting the AQUA satellite  
137 retrievals with the TERRA satellite, which is host to the same instruments as AQUA but has an overpass  
138 time of ~1030 LST. The two satellites are host to several instruments including MODIS, CERES  
139 (Clouds and the Earth's Radiant Energy System), and AIRS (The Atmospheric Infrared Sounder). The  
140 use of all three instruments, alongside reanalysis and precipitation datasets, provides spatially and  
141 temporally collocated data that can be used to support individual observations and strengthen the  
142 analysis. Additionally, CERES can provide collocated information on the top-of-atmosphere (TOA)  
143 radiative fluxes and the overall radiative effect of the smoke, which has not previously been explored  
144 in this region.

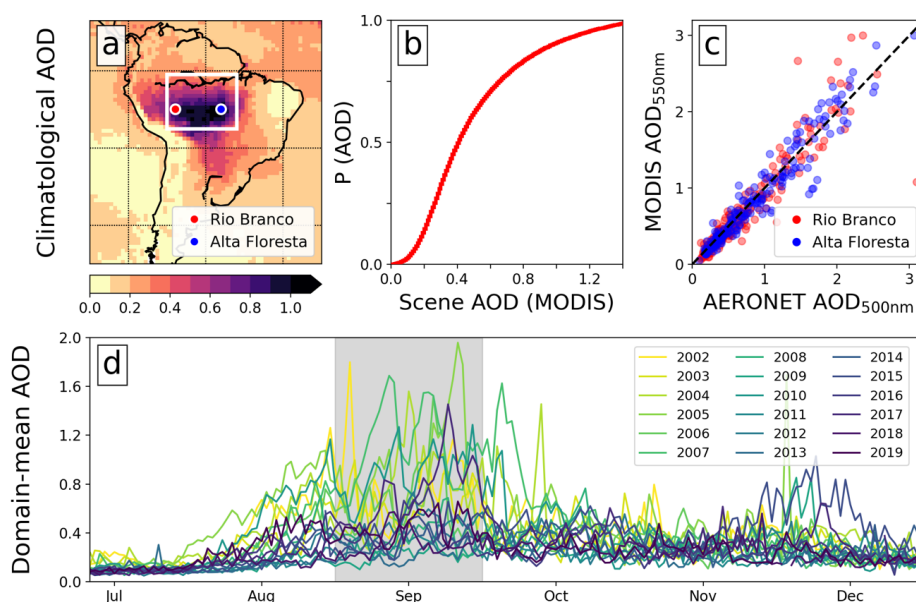


## 145 2. Methodology

### 146 2.1 Domain and Analysis Time Period

147 Biomass burning occurs annually during the dry season between the months of August and October  
148 (Figure 1d). We focus our analysis on the peak AOD month of September between 2002 and 2019, and  
149 confine the analysis to an area (70W to 52W, 15S to 1S) collocated with a region of climatologically  
150 high AOD Figure 1a), which we assume is dominated by smoke.

151  
152



153  
154 **Figure 1.** Information on the climatological AOD in the region during the analysis period of 2002 to 2019: (a)  
155 MODIS AOD climatology for September; (b) cumulative probability of occurrence of gridded MODIS AOD in  
156 the analysis domain (white box in a); (c) collocated AERONET and daily-mean MODIS retrieved AOD at the  
157 two stations shown in a; and (d) timeseries of daily-mean AOD from MODIS-AQUA over the analysis region  
158 (timeseries only shown between July and December for clarity). MODIS AODs are given at a wavelength of  
159 550nm and AERONET at 500nm.

### 160 2.2 Satellite and Reanalysis Products

161 In this study we primarily use data products from the MODIS, CERES, and AIRS instruments  
162 onboard AQUA and TERRA satellites. This is complemented by precipitation information from the  
163 Global Precipitation Measurement (GPM) level 3 Integrated Multi-satellitE Retrievals for GPM  
164 (IMERG) dataset, and meteorological information from ERA5 reanalysis. A brief overview of the  
165 variables extracted from each dataset is presented below, with full details in Table S1.

166

167 *MODIS AQUA and TERRA:* We use the MODIS collection 6.1 1-degree level 3 products (AQUA:  
168 MYD08\_D3 and TERRA: MOD08\_D3) for instantaneous retrievals of AOD (given at 550 nm) and  
169 cloud properties including total cloud fraction ( $CF_{total}$ ), liquid cloud fraction ( $CF_{liquid}$ ), LWP, IWP, total  
170 water path (TWP), cloud top temperature (CTT) and height (CTH), cloud optical thickness of both  
171 liquid and ice ( $COT_{total}$ ) and liquid only ( $COT_{liquid}$ ), ice cloud droplet effective radius ( $RE_{ice}$ ), and cirrus  
172 fraction ( $CF_{cirrus}$ ). The morning TERRA overpass is at  $\sim 1030$  LST and afternoon AQUA overpass at  
173  $\sim 1330$  LST.



174 *CERES top-of-atmosphere fluxes*: Top of atmosphere fluxes of radiation for the incoming solar  
175 ( $SOL_{TOA}$ ), shortwave ( $SW_{TOA}$ ), longwave ( $LW_{TOA}$ ), and net ( $NET_{TOA}$ ) components on a 1-degree grid  
176 are taken from the CERES level 3 data product, SSF1Deg-1H, that provides instantaneous fluxes  
177 onboard AQUA and TERRA satellites.

178

179 *AIRS*: The AIRS daily level 3 product, AIRS3STD, is used to provide daily mean values of total  
180 column water vapor ( $QV_{column}$ ), surface level specific humidity ( $QV_{surface}$ ), and surface level relative  
181 humidity ( $RH_{surface}$ ).

182

183 *IMERG precipitation*: Daily accumulated precipitation estimates ( $P_{accum}$ ) on a 0.1-degree grid are  
184 taken from the IMERG dataset (3B-DAY\_MS\_MRG\_3IMERG\_V06). A second dataset (3B-  
185 HHR\_MS\_MRG\_3IMERG\_V06B) provides 30-minute temporal resolution estimates at 0.1-degree  
186 resolution, used to determine cumulative precipitation in the morning ( $P_{AM}$ ; 0700 – 1200 LST),  
187 afternoon ( $P_{PM}$ ; 1400 – 1900 LST), and peak precipitation rate during the diurnal cycle ( $P_{peak}$ ).

188

189 *ERA5 Reanalysis*: Daily mean 850 hPa horizontal winds and 2m temperature ( $T_{2m}$ ) on a 1-degree  
190 grid are taken from the ERA5 reanalysis dataset for spatial collocation with satellite observations;  
191 horizontal wind components are used to determine the wind direction (degrees from due north). Daily  
192 mean fields of 850 hPa specific humidity ( $QV_{850}$ ) and temperature ( $T_{850}$ ) are also taken from the dataset  
193 to obtain large-scale environmental conditions upstream of the domain, discussed in Section 3.6; mean  
194 values are determined over a region off the east coast of South America (35W to 30W, 25S to 5N),  
195 roughly five days upstream of the prevailing winds (see supplementary material).

## 196 2.3 Collocating Datasets

197 All data is analysed on a regular 1-degree grid. MODIS, CERES, AIRS, and ERA5 datasets are  
198 provided on a 1-degree grid so are readily collocated spatially, and IMERG data is regridded onto a 1-  
199 degree grid. CERES instantaneous TOA fluxes and MODIS products each have separate datasets for  
200 TERRA and AQUA overpasses and are temporally collocated in the analysis. Daily mean ERA5  
201 horizontal winds, describing the large-scale daily-mean flow, are selected for each corresponding day  
202 of the timeseries, and daily mean AIRS and IMERG daily  $P_{accum}$  and  $P_{peak}$  data similarly selected.  $P_{AM}$   
203 and  $P_{PM}$  are collocated with the TERRA and AQUA datasets, respectively. Although AIRS provides  
204 instantaneous retrievals we use the retrieved atmospheric water variables to describe the large-scale  
205 environmental properties, and as such do not require the higher temporal resolution.

206

207 In this study we are primarily interested in how widespread properties of the atmosphere change with  
208 AOD. Representation error may arise from the fact that AOD retrievals are made in clear-sky  
209 conditions, whereas cloud properties are necessarily in cloudy sky. Wet scavenging is known to impact  
210 the column loading of aerosol (Gryspeerd et al., 2015), therefore can we be confident that the AOD  
211 retrievals are representative of the underlying conditions impacting the clouds? As precipitation  
212 predominantly occurs within the afternoon period a comparison of AOD retrieved in the TERRA and  
213 AQUA overpasses provides some information as to whether we may expect wet scavenging to be  
214 strongly influencing the AOD. Figure S1 in the supplementary material shows that there is very little  
215 systematic bias between the two overpasses, even though precipitation has likely occurred in some of  
216 the scenes, therefore giving us confidence that clear-sky retrievals of AOD are representative of the  
217 widespread AOD. A second source of potential bias may occur if AOD retrievals made in very cloudy  
218 conditions are being misclassified and biased high. In previous studies (e.g., Koren et al., 2004; Yu et  
219 al., 2007) scenes where cloud fraction exceeds 0.8 have been removed to avoid AOD retrieval  
220 uncertainty, yet in this study we do not in order to preserve the data and avoid potential bias to the  
221 properties of the cloud field. This ensures that we are considering the response of the atmosphere over  
222 the region as a whole, rather than a subset. If clouds were strongly influencing the retrieved AOD then

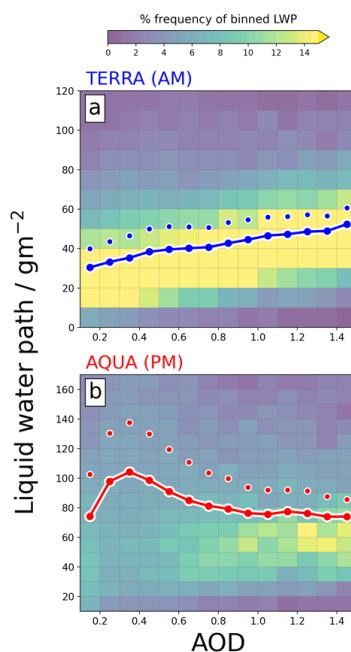


223 independent retrievals from AERONET, able to take measurements throughout the day, would highlight  
224 biases. A spatial and temporal collocated comparison of AOD retrieved from two AERONET stations  
225 (Rio Branco and Alta Floresta) with mean MODIS AOD shown in **Figure 1d** gives confidence that  
226 MODIS AOD retrievals are not biased high in the presence of high cloud coverage. This is consistent  
227 with the low biases reported by (Wei et al., 2019; Sayer et al., 2019), who additionally show evidence  
228 that South America has one of the lowest regional biases between the two datasets, partly due to the  
229 performance of the MODIS AOD retrievals over forested land. Previous studies (e.g., Koch and Del  
230 Genio, 2010) have shown that the position of smoke in relation to clouds can greatly impact the cloud  
231 rapid adjustments and ERF. A climatology of smoke plume heights over the Amazon presented by  
232 Gonzalez-Alonso et al. (2019) shows that during September smoke plumes are generally located below  
233 1.5 km, with less than 5 % of smoke plume injection heights observed in the free troposphere. Therefore,  
234 it is reasonable to assume that in our analysis, the smoke is largely situated within the boundary layer  
235 and interacting with the warm-phase cloud field.

### 236 3. Results

#### 237 3.1 Liquid Water Path

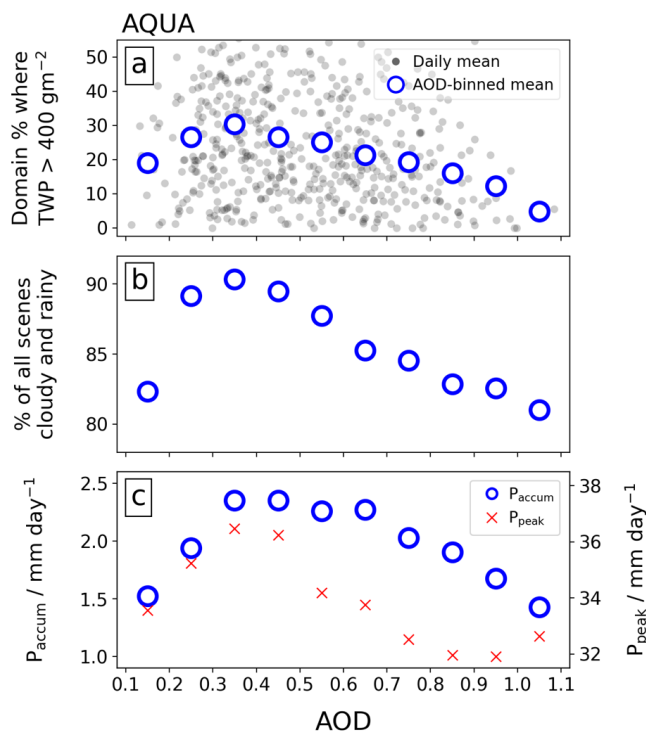
238 The 18-year September climatology shows that there are contrasting LWP-AOD relationships in the  
239 morning and afternoon. **Figure 2** shows a consistent increase in LWP with AOD for the morning  
240 overpass (panel a); the histogram suggests that the existing clouds become increasingly laden with water  
241 as AOD increases. Conversely, the afternoon overpass (panel b) shows an initial spread of the cloud  
242 distribution to higher LWP, followed by a gradual focus towards lower LWP. This behaviour describes  
243 an initial enhancement followed by gradual suppression. The same analysis, performed on the domain-  
244 mean dataset rather than the 1-degree grid, results in the same relationships (see Figure S2).  
245



246  
247 **Figure 2.** MODIS liquid water path as a function of AOD for the (a) morning TERRA overpass and (b) afternoon  
248 AQUA overpass. Joint-histograms show % frequency of LWP binned by AOD, and coloured lines (individual  
249 circles) show the geometric (arithmetic) mean in each AOD bin. Data is only shown for cloudy scenes where  
250 LWP > 0.



251 The contrasting diurnal responses of LWP to AOD are consistent with the high-resolution modelling  
252 study from Herbert et al. (2021). In their study it was found that the domain-mean LWP adjustment to  
253 an AOD perturbation was positive in the morning (due to widespread modification to the  
254 thermodynamic environment) but negative in the afternoon (due to a suppression of convection).  
255  
256



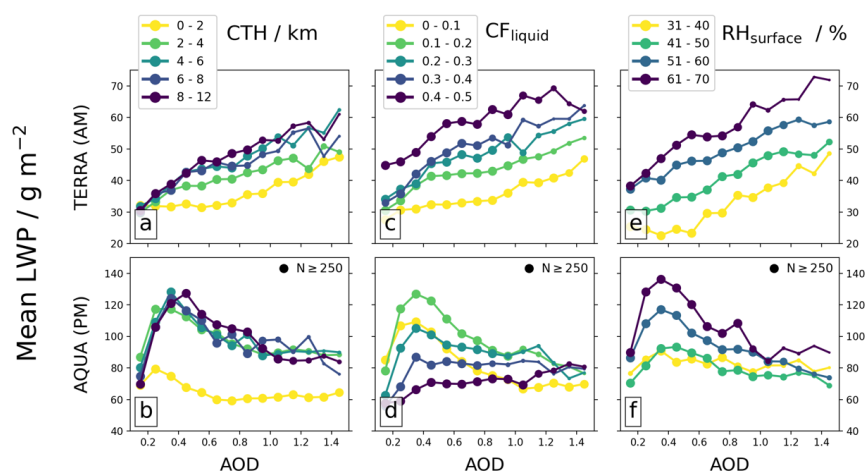
257 **Figure 3.** Convection and precipitation as a function of AOD: (a) percentage of the domain where TWP >  
258 400 gm<sup>-2</sup> as a function of the domain-mean AOD for each day (filled grey circles) and the mean of all days  
259 binned by AOD (empty blue circles); (b) mean percentage of all scenes that include liquid cloud and  
260 precipitation as a function of binned AOD; and (c) mean daily accumulated precipitation (blue circles) and daily  
261 peak precipitation (red crosses) in each scene binned by AOD. MODIS data is shown for the AQUA overpass.  
262

263

264 The enhanced mean LWP in the morning overpass (**Figure 2a**) is consistent with ACI-induced  
265 suppression of the warm-rain process, where an increase in CCN from smoke results in a more  
266 numerous, smaller, cloud droplets; this behaviour has been observed in observational (e.g., Twohy et  
267 al., 2021; Andreae et al., 2004; Martins and Silva Dias, 2009) and modelling (e.g., Liu et al., 2020;  
268 Herbert et al., 2021; Martins et al., 2009) studies. The afternoon AOD dependence in **Figure 2b** is well  
269 aligned with changes in the convective activity. An increase in CCN availability has been found to  
270 promote convection in some studies via ACI adjustments (Fan et al., 2018; Lebo, 2018; Khain et al.,  
271 2005; Marinescu et al., 2021), whilst the heat generated from biomass burning has also been found to  
272 enhance buoyancy and deep convection (Zhang et al., 2019). ARI adjustments from smoke also impact  
273 convection as the aerosol particles cool the surface and stabilise the boundary layer via elevated heating  
274 of the absorbing aerosol, acting to suppress convection. Using a theoretical model Koren et al. (2004)  
275 demonstrated that the competition between ACI and ARI adjustments in deep convective clouds results  
276 in an initial enhancement (driven by ACI) for small AOD perturbations, followed by a suppression at



277 higher AOD as ARI adjustments dominate. The observations in this study are consistent with this;  
278 **Figure 3a** demonstrates that the percentage of the domain that exhibits high TWP loadings (indicative  
279 of deep convective clouds) follows this non-linear relationship with AOD. **Figure 3b** and **Figure 3c**  
280 additionally show that the non-linearity is reflected in the occurrence of precipitating liquid clouds, and  
281 the magnitude of precipitation itself ( $P_{\text{accum}}$  and  $P_{\text{peak}}$ ). For  $\text{AOD} > 0.4$  there is less suppression in the  
282 precipitation (**Figure 3b** and **c**) compared to the fraction of domain that shows signs of convective  
283 activity (**Figure 3a**); this may suggest that at high AOD there are fewer deep convective cells but those  
284 that do form are more intense, providing relatively more precipitation per convective cell.  
285  
286



287  
288

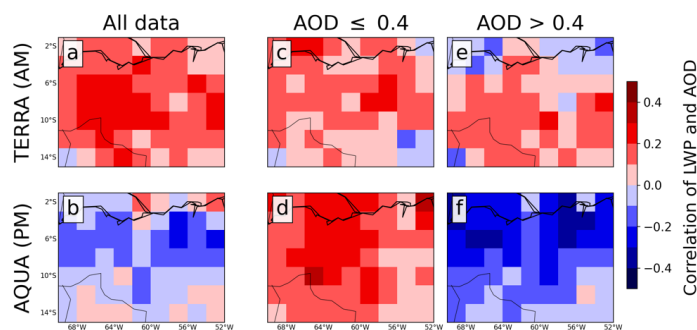
289 **Figure 4.** Geometric mean LWP as a function of AOD, subset by different cloud or environmental properties:  
290 MODIS cloud top height (**a – b**), MODIS liquid cloud fraction (**c – d**); and AIRS surface level RH (**e – f**). For  
291 each plot the top panel is for the TERRA overpass and bottom panel for the AQUA overpass. The size of each  
292 circle gives a representation of how many scenes are included in the mean, with a maximum size shown for  $N \geq$   
293 250.

294

295 Subsetting the dataset by CTH,  $CF_{\text{liquid}}$ , and  $RH_{\text{surface}}$  in **Figure 4** demonstrates that the LWP-AOD  
296 relationships observed in **Figure 2** persist when constrained by environmental conditions. For the  
297 morning TERRA overpass (**Figure 4** top row) the AOD-binned mean LWP increases with AOD for all  
298 constrained datasets. CTH (**Figure 4a**) and  $CF_{\text{liquid}}$  (**Figure 4b**) show interesting behaviour. For  $\text{AOD} <$   
299 0.4 LWP increases sharply for all clouds that extend beyond 2 km and exhibit  $CF_{\text{liquid}} > 0.2$ , which  
300 may indicate mesoscale systems that have persisted overnight. Above this AOD (where we posit  
301 daytime convection is being suppressed) the data is predominantly confined to small boundary layer  
302 clouds with  $CF_{\text{liquid}} < 0.1$  and  $\text{CTH} < 1$  km (the smaller marker sizes depict fewer data points),  
303 suggesting a link between convective activity during the daytime (**Figure 3**) and the development of  
304 larger mesoscale systems. Subsetting by  $RH_{\text{surface}}$  (**Figure 4c**) shows a consistent and positive LWP-  
305 AOD relationship, which suggests the increase in LWP is being driven by changes in cloud properties  
306 (ACI), rather than the environment. The AQUA overpass in the afternoon (**Figure 4** bottom row)  
307 provides more evidence that the mean response is controlled by the initial enhancement ( $\text{AOD} < 0.4$ )  
308 and then suppression ( $\text{AOD} > 0.4$ ) of convective activity. First, all clouds that exceed CTH of 2 km  
309 display an almost identical relationship with LWP (**Figure 4b**), with this subset of clouds typically  
310 representative of locations containing cells of deep convection. Second, lower  $CF_{\text{liquid}}$  scenes (**Figure**  
311 **4d**) show greater sensitivity to AOD and greater magnitudes of LWP. This can be explained by  
312 appreciating that deeper convective clouds will contain more cloud condensate in the ice phase, and



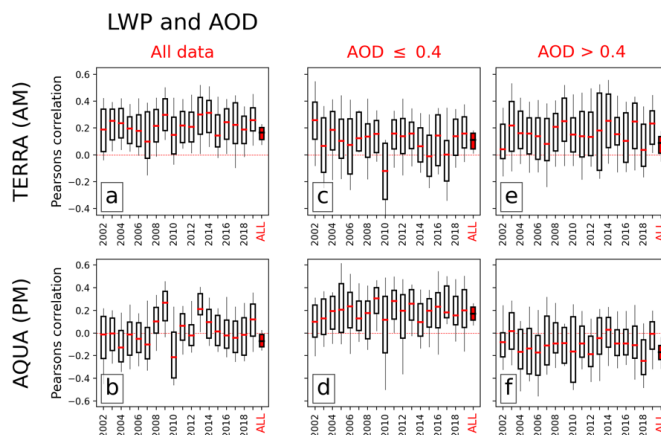
313 therefore not retrieved as liquid cloud (subsetting IWP by  $CF_{total}$  confirms this) – low  $CF_{liquid}$  scenes  
 314 with high loadings of LWP thereby indicate regions with intense convective cells. Subsetting by  
 315  $RH_{surface}$  demonstrates that the environmental conditions play a role in the LWP-AOD relationship, and  
 316 is likely mediated by the connection between boundary layer moisture, CAPE, and convective activity  
 317 (a similar relationship was observed by Ten Hoeve et al. (2011) for  $COT_{liquid}$ ). The response of  $RH_{surface}$   
 318 to AOD will be discussed in Section 3.4.  
 319



320  
 321 **Figure 5.** Pearson's correlation coefficient between LWP and AOD. Top row (a, c, e) shows the TERRA overpass  
 322 in the morning, and bottom row (b, d, f) shows the AQUA overpass in the afternoon. Left column (a and b) shows  
 323 the spatial distribution of the coefficient for all data, middle column (c and d) shows data for  $AOD \leq 0.4$ , and  
 324 right column (e and f) shows data for  $AOD > 0.4$ . Red colours depict a positive correlation, blue colours a negative  
 325 correlation.

326 Is this response spatially consistent? If not it may suggest we are seeing different regions of the  
 327 domain influencing the mean and masking any underlying AOD relationship. **Figure 5** shows the  
 328 Pearson's correlation coefficient between LWP and AOD across the domain (regridged from 1-degree  
 329 to 2-degree resolution to increase the number of datapoints). The TERRA correlation apparent in **Figure**  
 330 **2a** suggests a consistent positive relationship throughout the range of AOD, which is also observed  
 331 across the domain in **Figure 5a** with positive (albeit small) correlation coefficients throughout. For the  
 332 AQUA overpass we also see a consistent correlation as observed in **Figure 2**: for  $AOD \leq 0.4$  the  
 333 correlation is consistently positive across the domain (**Figure 5d**), and  $AOD > 0.4$  is consistently  
 334 negative throughout the domain (**Figure 5f**).

335



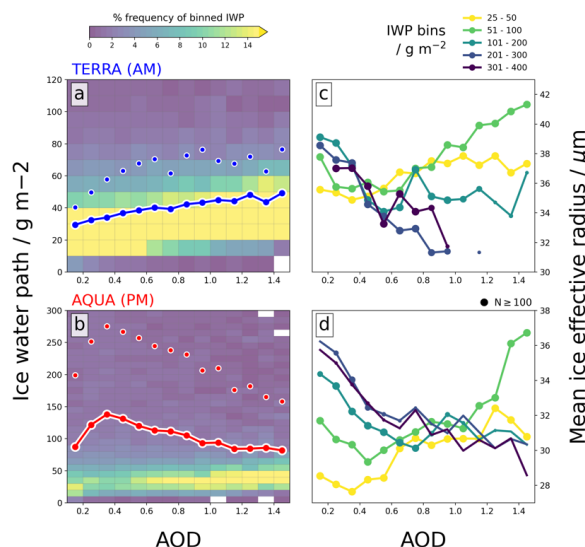
336  
 337 **Figure 6.** Boxplots showing Pearson's correlation coefficients in the domain, for the September of each individual  
 338 year during the timeseries. Rows and columns as in **Figure 5**. Right-most boxplot (in red) in each subplot shows  
 339 the data for all years.



340 The interannual variability in the LWP-AOD relationship during September is shown in **Figure 6**  
341 (also see Figure S3). Here the correlation coefficients are similarly determined throughout the domain  
342 (as in **Figure 5**) but now data is additionally subset for each year. The TERRA overpass shows a positive  
343 LWP-AOD relationship (for all AOD) over the entire timeseries (**Figure 6a**) with some degree of  
344 interannual variability. Note the final boxplot using the entire 18-year timeseries, demonstrating the  
345 benefit of using a long timeseries. The AQUA afternoon overpass shows more interannual variability,  
346 though still shows a consistent relationship below (**Figure 6d**) and above  $\text{AOD} = 0.4$  (**Figure 6f**). A  
347 possible explanation for the additional variability is if the LWP response is connected to the  
348 enhancement or suppression of convective cells; the CAPE and other environmental conditions required  
349 for triggering deep convection would be sensitive to larger-scale drivers and thus influence the number  
350 of convective cells on any given day, month, and year. As shown in **Figure 4f** the LWP response in the  
351 afternoon is particularly sensitive to the  $\text{RH}_{\text{sfc}}$  (moisture content is a key component of CAPE). In  
352 Section 3.6 we will provide evidence that suggests the LWP-AOD relationships presented here are not  
353 driven by large-scale external drivers, and are primarily an internalised response to AOD.

### 354 3.2 Ice Water Path and Effective Radius

355 The simulations from Herbert et al. (2021) showed pronounced increases in IWP and ice-cloud  
356 coverage which had important implications for the longwave TOA radiative effect due to smoke. **Figure**  
357 **7** shows the mean IWP and  $\text{RE}_{\text{ice}}$  retrieved from MODIS binned by AOD. For the IWP in the morning  
358 overpass (**Figure 7a**) there is an overall positive relationship with  $> 50\%$  increase in IWP from  
359  $\text{AOD} = 0.2$  to  $\text{AOD} = 1.0$ . The AQUA overpass (**Figure 7b**) shows initial enhancement of IWP up to  
360  $\text{AOD} = 0.4$  followed by a consistent negative relationship. In both timeframes, the geometric mean  
361 displays a maximum IWP response to AOD of  $+50\%$ , though there is considerably more sensitivity to  
362 AOD in the afternoon. This behaviour is closely correlated with the LWP-AOD relationships (**Figure**  
363 **2**). Enhanced LWP in the morning from a suppressed warm-rain process allows more condensate to  
364 reach the freezing level, and in the afternoon changes in convective activity will have a direct influence  
365 on the amount of condensate reaching the freezing level.  
366



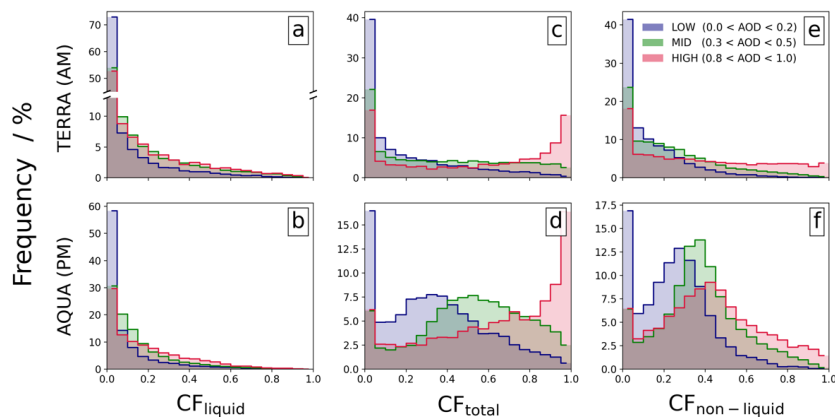
367 **Figure 7.** MODIS ice water path (IWP) as a function of AOD (**a** and **b**) and MODIS mean ice effective radius  
368 binned by IWP as a function of AOD (**c** and **d**) for the TERRA (top row) and AQUA overpasses (bottom row).  
369 Joint-histograms show % frequency of IWP binned by AOD, and coloured lines (individual circles) show the  
370 geometric (arithmetic) mean in each AOD bin.  
371



372  $RE_{ice}$  provides information on the cloud-top ice particle size distribution; **Figure 7c** and **Figure 7d**  
373 show mean  $RE_{ice}$  as a function of AOD for bins of IWP. For  $AOD < 0.4$   $RE_{ice}$  decreases with AOD for  
374 all IWP bins during both overpasses, whilst at  $AOD > 0.4$   $RE_{ice}$  increases for low IWP scenes, and  
375 continues to decrease for high IWP scenes. This behaviour suggests that for deep convective clouds  
376 associated with high IWP, increasing AOD and the availability of CCN results in smaller ice particle  
377 sizes at the cloud-top. A possible explanation is ACI effects resulting in a larger CDNC of smaller  
378 droplet sizes at the freezing level; smaller ice particles increase the longevity of deep convective outflow  
379 and high-altitude cloud coverage (Wendisch et al., 2016). Lower IWP scenes ( $< 100 \text{ g m}^{-2}$ ) generally  
380 show an increasing  $RE_{ice}$  with AOD; these scenes may be associated with weakly convective regions  
381 dominated by shallower convection. This contrasting behaviour is consistent with Zhao et al. (2019)  
382 who found ice particle size decreased for strongly convective regions, and increased for moderately  
383 convective regions (when going from clean to polluted conditions), which occurred due to the different  
384 freezing pathways dominant in each type of convection.  
385

### 386 3.3 Cloud Fraction

387 Changes to the cloud coverage over a region strongly influences the TOA radiative response.  
388 Subsetting  $CF_{liquid}$  and  $CF_{total}$  to low ( $0.0 < AOD < 0.2$ ), mid ( $0.3 < AOD < 0.5$ ), and high-AOD ( $0.8 <$   
389  $AOD < 1.0$ ) scenes in **Figure 8** demonstrates widespread modifications to the cloud field over the  
390 region, alongside the changes in LWP.  
391



392 **Figure 8.** Normalized probability of occurrence of  $CF_{liquid}$  (a – b),  $CF_{total}$  (c – d) and  $CF_{non-liquid}$  (e – f) for low ( $0.0$   
393  $< AOD < 0.2$ ), mid ( $0.3 < AOD < 0.5$ ) and high ( $0.8 < AOD < 1.0$ ) AOD scenes. Top row shows the TERRA  
394 overpass in the AM, and the bottom row shows the AQUA overpass in the PM. Note the break in the y-axis in  
395 panel (a).  
396

397  
398 The relative percentage of cloud-free scenes ( $CF < 0.05$ ) in both overpasses and all cloud phases  
399 strongly decrease for  $AOD > 0.2$ .  $CF_{liquid}$  in the morning (**Figure 8a**) is well aligned with LWP (**Figure**  
400 **2a**) and a suppression of precipitation, promoting cloudiness. There is little change going from mid to  
401 high-AOD scenes suggesting a saturation effect of  $CF_{liquid}$ , though the cloud LWP (**Figure 2a**) continues  
402 to increase; this could be associated with a widespread and robust drying of the boundary layer as AOD  
403 increases (see Section 3.4). In the afternoon  $CF_{liquid}$  is similarly well-correlated with the LWP-AOD  
404 relationship and convective activity. For mid-AOD scenes the enhanced convection drives an increased  
405 frequency of liquid cloud coverage over much of the distribution (**Figure 8b**). At higher AOD loadings  
406 there is a suppression of convection which promotes the occurrence of liquid cloud retrievals  
407 (fewer/weaker convective cells results in reduced mixed-phase cloud coverage). This result may have



408 important implications for the TOA radiative response as liquid clouds are more radiatively opaque than  
409 ice clouds (Cesana and Storelvmo, 2017).

410

411  $CF_{\text{total}}$  (**Figure 8 c – d**) demonstrates widespread sensitivity of the Amazon to the presence of AOD,  
412 with clear shifts in the cloud field distribution that correlate with the changes in convective activity.  
413  $CF_{\text{non-liquid}}$  ( $CF_{\text{total}} - CF_{\text{liquid}}$ ) provides information on the non-liquid phase cloud coverage (**Figure 8 c –**  
414 **f**). Beginning with the afternoon overpass (**Figure 8d**), low AOD scenes are characterised by ~85%  
415 cloud coverage, with a peak centered around  $CF_{\text{total}} = 0.3$ ; this likely correlates with the presence of  
416 scattered deep convective cells that extend beyond the freezing level. As convective activity increases  
417 with AOD (**Figure 3**) the domain becomes cloudier, and the peak occurrence (for mid-AOD) shifts to  
418 higher coverage as enhanced convection promotes more numerous / intense cells, increasing the cloud  
419 coverage. For high-AOD scenes the convection is suppressed, promoting the occurrence of extensive  
420  $CF_{\text{total}}$  coverage exceeding 0.8 (aerosol misclassification of cloud was discussed in Section 2.3, and we  
421 do not believe it is heavily influencing the coincident high-AOD and high- $CF_{\text{total}}$  scenes).  $CF_{\text{non-liquid}}$   
422 (**Figure 8f**) shows that although convection is suppressed in the high-AOD scenes (lower peak) there is  
423 still some convective activity with a peak centered at higher cloud coverages, which suggests that under  
424 high-AOD conditions deep convection is less likely, but when it does occur it is more intense. This may  
425 explain why mean  $P_{\text{accum}}$  remains relatively enhanced for  $AOD > 0.4$  (**Figure 3b and c**) even though  
426 convective activity is less likely (**Figure 3a**), though would require more attention to confirm.  $CF_{\text{non-}}$   
427  $liquid$  demonstrates that the extensive  $CF_{\text{total}}$  coverage under high-AOD conditions in **Figure 8d** is driven  
428 by a combination of liquid and non-liquid clouds, and not solely due to extensive cirrus clouds or deep  
429 convective anvil outflow. The morning overpass  $CF_{\text{total}}$  and  $CF_{\text{non-liquid}}$  (**Figure 8c and e**) bear strong  
430 similarities to the afternoon overpass: at low AOD there are preferentially more low-coverage scenes,  
431 and at high AOD there are preferentially more high-coverage scenes. The sensitivity to AOD is  
432 primarily driven by the non-liquid phase and likely associated with the previous day's convective  
433 activity; this is most evident under high-AOD scenes and may indicate longer-lived convective systems  
434 or more intense cells. The pronounced shift from low to high  $CF_{\text{total}}$  occurrence with AOD during both  
435 overpasses (**Figure 8c and d**) is a consistent feature for all years when individually analysed (see **Figure**  
436 **S4**), which suggests this is a causal relationship, rather than an artefact of co-varying meteorology which  
437 is more likely to exhibit interannual variability. This will be explored further in Section 3.6.

### 438 3.4 Large-scale Environment

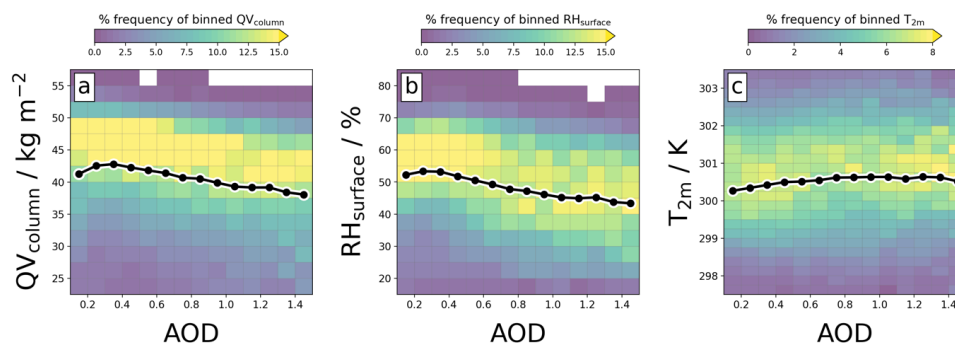
439 Changes to the large-scale environments of moisture availability and temperature can influence the  
440 formation and evolution of clouds and precipitation. Studies have demonstrated that smoke  
441 perturbations may drive widespread changes to these properties (e.g., Yu et al., 2007; Zhang et al.,  
442 2008b; Lee et al., 2014; Herbert et al., 2021), thus influencing the overall response of the cloud field.

443

444 AIRS observations of total column water vapour ( $QV_{\text{column}}$ ) and relative humidity at the surface  
445 ( $RH_{\text{surface}}$ ), together with ERA5 reanalysis data of the 2-metre temperature ( $T_{2m}$ ) are collocated with  
446 AOD in **Figure 9**. The observations suggest that the moisture content of the column and boundary layer  
447 (BL) generally decrease as AOD increases, though there is an initial increase at low AOD values.  
448  $QV_{\text{column}}$  will be primarily influenced by local changes in precipitation and surface fluxes that modify  
449 the water content of the BL. As observed in **Figure 3** and **Figure 4** there is an increase in convection  
450 and precipitation until  $AOD = 0.4$ , followed by a decrease. This relationship correlates well with the  
451  $QV_{\text{column}}$  sensitivity to AOD in **Figure 9a**, though there is more evident suppression of  $QV_{\text{column}}$  than  
452  $P_{\text{accum}}$ . This may be caused by surface cooling (due to the smoke) reducing surface fluxes of moisture  
453 (Zhang et al., 2008b), thus enhancing the drying of the BL. The sensitivity of  $RH_{\text{surface}}$  is strongly  
454 influenced by  $QV_{\text{column}}$  and displays a similar relationship though suppression at higher values of AOD  
455 is more pronounced, possibly due to an overall warming of the BL.  $T_{2m}$  from ERA5 increases as a  
456 function of the AOD; smoke strongly absorbs solar radiation and results in anomalous heating which



457 may explain the increase, however,  $T_{2m}$  only increases by  $\sim 0.5$  K over the whole range of AODs which  
458 suggests other sources influence the temperature. Surface cooling due to the overlying smoke will  
459 reduce the surface sensible heat flux, which may counteract some of the heating. The collocated data  
460 show that the large-scale environment changes alongside the AOD, and is likely driven by changes to  
461 the convective activity over the region and changes to surface fluxes due to ARI processes. The  
462 influence of large-scale external drivers to these conclusions are discussed in Section 3.6.  
463



464 **Figure 9.** Daily mean (a) AIRS total column water vapour ( $QV_{column}$ ), (b) AIRS surface RH ( $RH_{surface}$ ), and (c)  
465 ERA5 2-metre temperature ( $T_{2m}$ ) as a function of AOD. Joint-histograms show % frequency of each variable  
466 binned by AOD, and black lines show the mean in each AOD bin.  
467

468

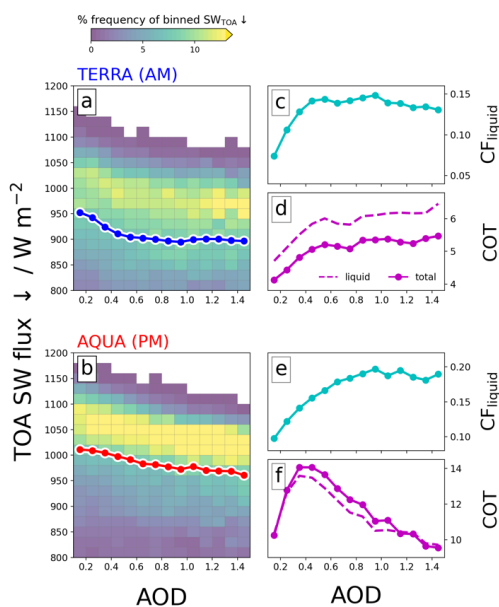
### 469 3.5 Top-of-atmosphere radiative effects

470 Collocated all-sky CERES retrievals from both TERRA and AQUA overpasses provide us with the  
471 TOA radiative impact of smoke and a means to corroborate previous findings from the MODIS  
472 retrievals.

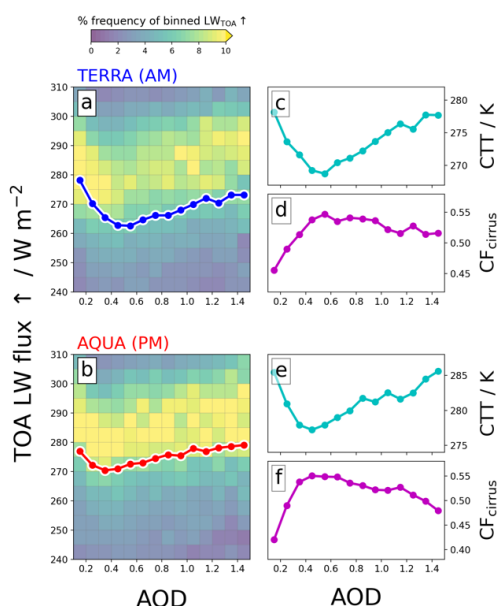
473

474 The  $SW_{TOA}$  flux is largely determined by the underlying albedo, so is function of the cloud fraction,  
475 cloud optical thickness, AOD, and surface albedo. **Figure 10** shows increases in AOD are correlated  
476 with a decrease in net downwards  $SW_{TOA}$  (cooling) with a maximum cooling effect of  $50 \text{ Wm}^{-2}$  in both  
477 time periods. In clear-sky conditions extinction from smoke aerosol results in less solar radiation at the  
478 surface and increases outgoing SW radiation. A 1D radiative transfer model (ecRad; Hogan and Bozzo,  
479 2018) was used to estimate the TOA SW radiative effects due to smoke in the presence of clouds over  
480 the Amazon; output is shown in Figure S5 in the supplementary material. For a typical smoke  $SSA_{550nm}$   
481 of 0.92 over the region (Palácios et al., 2020; Rosário et al., 2011) an AOD perturbation of 1.5 results  
482 in a  $SW_{TOA}$  clear-sky instantaneous aerosol radiative effect on the order of  $-40 \text{ Wm}^{-2}$ , but is strongly  
483 offset towards positive values when even small cloud coverage is present (see Figure S5). Therefore,  
484 although the presence of smoke aerosol is potentially contributing towards the negative correlation in  
485  $SW_{TOA}$  the changes to cloud properties are likely the primary driver of the observed relationship.  
486

487 The morning relationship is largely driven by the change in  $CF_{liquid}$  across the domain (**Figure 10c**)  
488 which increases by +100% at  $AOD = 0.5$  then slowly decreases. COT (**Figure 10d**) gradually increases  
489 with AOD, and is largely controlled by the change in  $CF_{liquid}$  and the increase in cloud LWP (**Figure 2**).  
490 The afternoon overpass shows a consistent increase in the outgoing  $SW_{TOA}$  with AOD but of smaller  
491 magnitude than in the morning. The relationship is well correlated with the MODIS-retrieved  $CF_{liquid}$   
492 and COT that have contrasting trends (**Figure 10e** and **f**);  $CF_{liquid}$  consistently increases with AOD,  
493 whereas for  $AOD > 0.4$  COT counteracts these changes, resulting in a weakly decreasing  $SW_{TOA}$   
494 correlation.  
495



496  
 497 **Figure 10.** CERES TOA net downward SW flux as a function of AOD (a – b) for the morning TERRA overpass  
 498 (a) and afternoon AQUA overpass (b). Joint-histograms show % frequency of  $SW_{TOA}$  binned by AOD, and  
 499 coloured lines show the mean in each AOD bin. Column on the right (c – f) shows MODIS retrieved mean  $CF_{liquid}$   
 500 (c, e) and mean COT (d, f) binned by AOD for the corresponding satellite overpasses. COT is shown for both  
 501  $COT_{total}$  (solid) and  $COT_{liquid}$  (dashed).



502  
 503 **Figure 11.** CERES outgoing TOA longwave flux as a function of AOD (a – b) for the morning TERRA overpass  
 504 (a) and afternoon AQUA overpass (b); joint-histograms show % frequency of  $LW_{TOA}$  binned by AOD, and  
 505 coloured lines show the mean in each AOD bin. Column on the right (c – f) shows MODIS retrieved mean cloud  
 506 top temperature (c, e) and cirrus fraction (d, f) binned by AOD for the corresponding satellite overpasses.

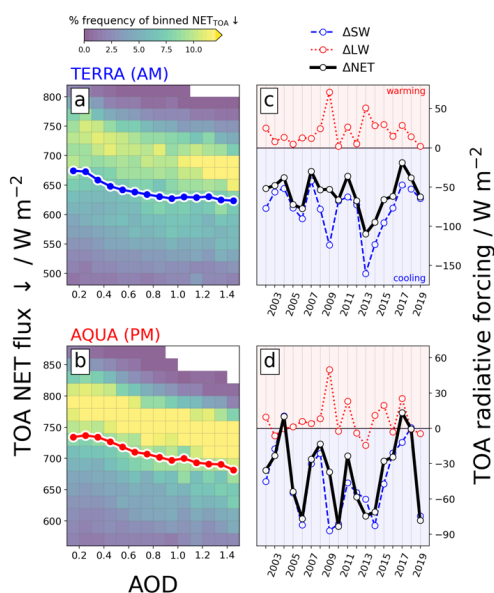


507 These results provide evidence that the  $SW_{TOA}$  radiative effect from smoke is strongly influenced by  
 508 the widespread changes to the cloud regimes in the region via ACI and ARI rapid adjustments. The 2d-  
 509 histograms in **Figure 10** show considerably more variability in the TERRA overpass than in the AQUA  
 510 overpass, suggesting that the background-state of the cloud field and environment in the morning plays  
 511 an important role in how it responds to the smoke. Conversely, the afternoon is more centered around  
 512 the impact to the convection.

513

514 Changes to the outgoing  $LW_{TOA}$  flux will be driven by modification to column-integrated phases of  
 515 water, and their vertical distribution. **Figure 11** shows considerable non-linear behaviour between  
 516  $LW_{TOA}$  and AOD, apparent in both satellite overpasses. Initially mean  $LW_{TOA}$  decreases with AOD until  
 517  $AOD \approx 0.4$ , then increases. The relationship is more apparent in the morning (**Figure 11a**) than in the  
 518 afternoon (**Figure 11b**) with reductions in  $LW_{TOA}$  of  $-20 \text{ W m}^{-2}$  and  $-10 \text{ W m}^{-2}$ , respectively. The  
 519 behaviour is well explained by the change in MODIS-retrieved CTH, which also correlate well with  
 520  $CF_{\text{cirrus}}$ . The  $CF_{\text{cirrus}}$ -AOD relationship in both overpasses (**Figure 11d** and **f**) is a result of both modified  
 521 convective activity in the afternoon (**Figure 3**) and changes to the cloud-top  $RE_{\text{ice}}$  (**Figure 7c** and **d**).  
 522 At  $AOD < 0.4$  convection is enhanced and smaller ice particles drive extensive long-lived cirrus clouds,  
 523 whilst at higher AOD convection is suppressed (or less frequent) and ice particle sizes tend to be larger,  
 524 resulting in lower cirrus coverage. The different magnitudes in  $LW_{TOA}$  appear to be a feature of the  
 525 diurnal cycle, with colder mean CTT in the morning than in the afternoon (**Figure 11c** and **e**) driving a  
 526 stronger sensitivity to AOD for the same decrease in CTT. An interesting feature occurs at high AOD:  
 527 the mean CTT in both overpasses is the same maximum value at very low and very high AOD, yet  
 528  $CF_{\text{cirrus}}$  does not return to the same coverage. This may be a result of ARI processes heating the smoke  
 529 layer and environment, increasing the CTT. The  $LW_{TOA}$  results demonstrate that convective activity in  
 530 the afternoon (and modifications as result of smoke) produces long-lived cirrus anvil clouds that persist  
 531 throughout the night, driving the observed  $LW_{TOA}$ -AOD relationship in the morning.

532



533

534 **Figure 12.** CERES TOA net incoming flux as a function of AOD (**a – b**) for the morning TERRA overpass (**a**)  
 535 and afternoon AQUA overpass (**b**); joint-histograms show % frequency of  $NET_{TOA}$  binned by AOD, and coloured  
 536 lines show the mean in each AOD bin. Column on the right (**c – d**) shows the September mean TOA radiative  
 537 forcing (from  $0.0 < AOD < 0.2$  to  $0.8 < AOD < 1.0$ ) for SW, LW, and NET components; negative values represent  
 538 a cooling and vice versa.

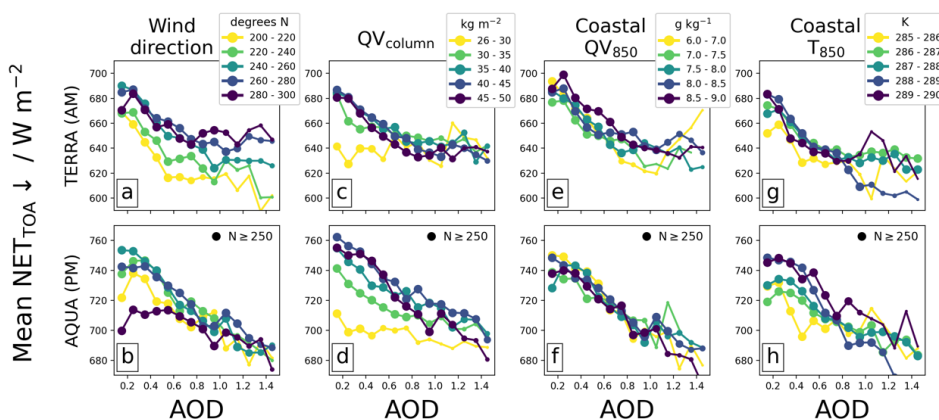


539  $NET_{TOA}$  fluxes and their relationship with AOD are shown in **Figure 12**. The nonlinearity of  $SW_{TOA}$   
 540 and  $LW_{TOA}$  largely counteract each other, resulting in a consistent and largely linear negative  
 541 relationship between  $NET_{TOA}$  and AOD (**Figure 12a** and **b**). In both overpasses the mean NET flux  
 542 reduces by  $\sim 50 \text{ Wm}^{-2}$  when  $AOD = 1$ , which represents a considerable aerosol radiative forcing and  
 543 pronounced cooling effect in this region.  
 544

545 The interannual variability of  $SW$ ,  $LW$  and  $NET$  components of the radiative forcing (RF) calculated  
 546 between  $0.0 < AOD < 0.2$  and  $0.8 < AOD < 1.0$  are shown in **Figure 12c** and **d**.  $RF_{NET}$  is consistently  
 547 negative in the AM and largely negative in the PM throughout the timeseries, though there is clearly  
 548 some interannual variability in the latter timeframe. The components  $RF_{SW}$  and  $RF_{LW}$  oppose each other,  
 549 with the  $LW$  warming from enhanced anvil coverage acting to partially counteract the  $SW$  cooling from  
 550 changes to the liquid cloud coverage and optical thickness, though  $RF_{SW}$  dominates the  $RF_{NET}$   
 551 magnitude and variability. The RF components suggest that changes to anvil properties ( $LW$ ) plays a  
 552 minor role, yet a comparison with **Figure 10** and **Figure 11** show that below  $AOD = 0.4$  the cooling is  
 553 primarily driven by the changes in liquid cloud ( $SW$ ), whereas for higher loadings of AOD the reduction  
 554 in anvil coverage ( $LW$ ) has a more pronounced role in driving the relationship. Additionally, the  $LW$   
 555 warming will dominate the radiative effect during the night, and may play a more important role in the  
 556 full diurnal cycle, though likely not to the extent as estimated for deep convection over tropical oceans  
 557 (Koren et al., 2010a).

### 558 3.6 Internalised response vs external drivers

559 An important question to ask is whether the sensitivity of the environment to AOD presented here is  
 560 a result of an internal response of the atmosphere over the Amazon rainforest, or an artefact of large-  
 561 scale driving meteorological conditions. These conditions may be seasonal-scale perturbations to the  
 562 transport of temperature and moisture to the region, or shifts in the climatological mean wind direction,  
 563 that result in drought susceptible conditions that may be more favourable for high AOD. In this event  
 564 the sensitivity of AOD and the widespread transition of cloud regimes that we have presented here may  
 565 be flawed.  
 566



567  
 568 **Figure 13.** Mean  $NET_{TOA}$  as a function of AOD subset by wind direction from due north (**a – b**) where  $270^\circ$   
 569 describes an easterly, total column water vapour (**c – d**), mean water vapour content of the coastal boundary layer  
 570 (**e – f**), and mean temperature of the coastal boundary layer (**g – h**). Top row is for the TERRA overpass and  
 571 bottom row for the AQUA overpass. The size of each circle gives a representation of how many scenes are  
 572 included in the mean, with a maximum size shown for  $N \geq 250$ .

573  
 574



575 Climatologically, the Amazon rainforest in September is characterised by easterlies that supply the  
576 region with moisture from the Atlantic Ocean (see Figure S6a). Southerly winds originating from over  
577 the continent may result in anonymously dry air, driving anomalous meteorological conditions and high  
578 AOD. **Figure 13a** and **b** show the AOD-binned  $\text{NET}_{\text{TOA}}$  subset by ERA5 collocated wind direction,  
579 ranging from northeasterlies ( $200^\circ\text{N}$ ) to southeasterlies ( $300^\circ\text{N}$ ). The subsetted data show that the  
580 cooling trend in  $\text{NET}_{\text{TOA}}\text{-AOD}$  is present for all wind directions, though there is variation in the  
581 magnitude, most notably in the AQUA afternoon overpass where winds other than easterlies result in a  
582 weaker cooling effect. A histogram of  $\text{QV}_{\text{column}}$  as a function of wind direction (Figure S7) shows that  
583 northerly and southerly winds exhibit lower loadings of water than easterlies. As the cooling trend in  
584 the afternoon is driven by changes in convection, it is likely that the drier air masses tend to produce  
585 weaker background convective activity as CAPE is reduced, and therefore weaken the sensitivity of the  
586 environment to AOD perturbations. This result is similarly observed when the  $\text{NET}_{\text{TOA}}$  is subset by  
587 AIRS  $\text{QV}_{\text{column}}$  in **Figure 13c** and **d**: the cooling trend persists but is weaker for drier airmasses,  
588 especially for  $\text{QV}_{\text{column}} < 35 \text{ kg m}^{-2}$ .

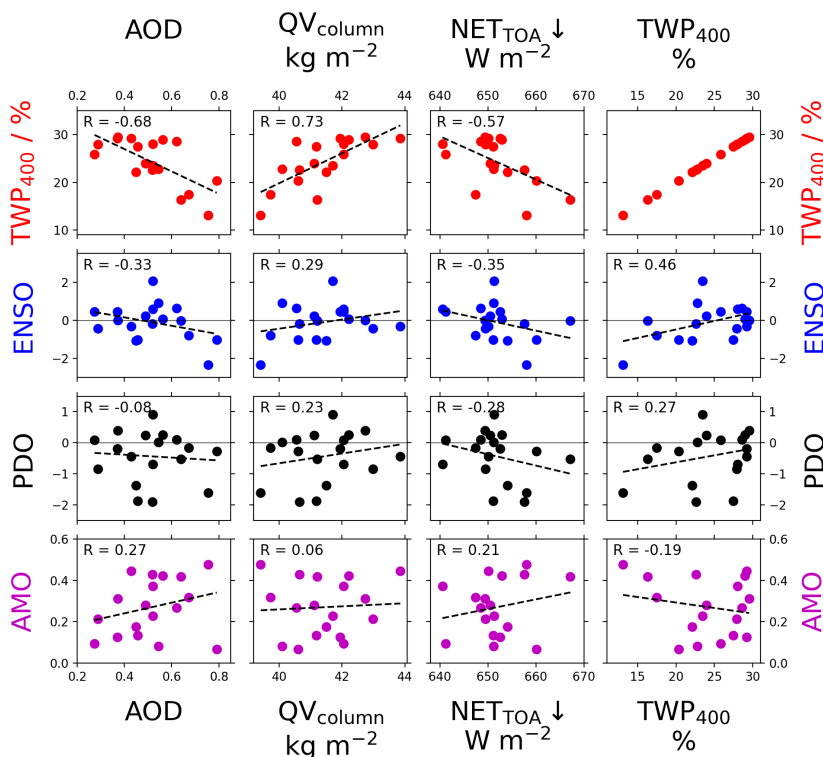
589 Collocated meteorological variables (e.g., moisture, winds) may be influenced by the presence of  
590 aerosol, weakening the robustness of the analysis. To account for this, we can subset the data for the  
591 large-scale meteorology influencing the region. Data is constrained for climatological easterlies that  
592 constitute 50% of the most frequent wind directions (Figure S6a), giving us some confidence that air  
593 advected into the region comes from the Atlantic coast. A region due east of the analysis domain off  
594 the coast (Figure S6b) is used to determine mean meteorological properties from ERA5, including  
595 temperature and water vapour content at 850 hPa ( $T_{850}$  and  $\text{QV}_{850}$ ); using coastal values removes any  
596 influence from the land-surface and associated processes. Back-trajectory analysis using the Hybrid  
597 Single-Particle Lagrangian Integrated Trajectory (HYSPPLIT) model (Stein et al., 2015) shows that air  
598 parcels in the analysis domain tend to originate in the boundary layer in the coastal region (hence 850  
599 hPa), taking  $\sim 5$  or more days to reach the domain. We therefore temporally collocate the constrained  
600 satellite dataset with mean  $T_{850}$  and  $\text{QV}_{850}$  from the coastal domain with an offset of -5 days. **Figure 13**  
601 **(e – h)** shows the AOD-binned mean  $\text{NET}_{\text{TOA}}$  subset by  $\text{QV}_{850}$  and  $T_{850}$  at the coast. The data, spanning  
602  $3 \text{ g kg}^{-1}$  and 5 K, shows a consistent cooling trend with almost no variation from  $\text{QV}_{850}$  and slightly  
603 weaker cooling for lower  $T_{850}$  (cooler advected air may reduce CAPE); this analysis supports the  
604 previous results.  
605  
606

607 In the final analysis, we look at the influence of climate-scale circulation anomalies/patterns such as  
608 ENSO, PDO and the AMO. El Niño Southern Oscillation (ENSO) is largely a phenomenon that impacts  
609 the Pacific Ocean though there have been links made between drought conditions in the Amazon and  
610 positive phases of the ENSO (Jimenez et al., 2021; Jiménez-Muñoz et al., 2016; Aragão et al., 2018).  
611 Similarly, the Pacific Decadal Oscillation (PDO) has also been linked to influencing the Amazon dry  
612 season (Aragão et al., 2018). The Atlantic Multidecadal Oscillation (AMO) impacts tropical Atlantic  
613 sea surface temperatures and the position of the Intertropical Convergence Zone, which can drive  
614 drought conditions over the Amazon (Boulton et al., 2022; Ciemer et al., 2020; Yoon and Zeng, 2010).  
615 If strong correlations between these phenomena and the AOD over the domain are evident, this would  
616 mean it is difficult to separate the two. Conversely, if there is no clear evidence of the phenomena  
617 driving the AOD variability then this would suggest that changes to the cloud field and environment  
618 (with respect to AOD) are more heavily influenced by local perturbations – i.e., the smoke. The same  
619 applies with other variables such as the  $\text{QV}_{\text{column}}$  or  $\text{RH}_{\text{surface}}$ . **Figure 14** shows the September mean  
620 AOD,  $\text{QV}_{\text{column}}$ , and  $\text{NET}_{\text{TOA}}$  each year of the timeseries as a function of the corresponding ENSO, PDO  
621 and AMO indices (averaged over August and September). There are no strong correlations evident for  
622 any pairings, and the strongest correlations are at odds with what we would expect. For example,  
623 positive ENSO years are generally associated with drought conditions, yet we observe lower AOD and  
624 lower  $\text{QV}_{\text{column}}$ . Although the sample size is small, this does suggest that the AOD is driven by localised  
625 processes, such as anthropogenic sources, rather than large-scale circulation anomalies. Similarly, the



626  $QV_{\text{column}}$  is not significantly influenced by these phenomena, and possibly primarily driven by local  
 627 sources of moisture. Although this is not an extensive nor entirely quantitative analysis we would expect  
 628 there to be more correlation if these large-scale circulation anomalies were driving the strong responses  
 629 that are evident from the MODIS, AIRS and CERES collocated retrievals. AIRS collocated data  
 630 (Figure 9) show that low AOD scenes are typically more moist than high-AOD scenes.  $RH_{\text{surface}}$   
 631 decreases more rapidly with AOD than  $QV_{\text{column}}$  which suggests temperature is also increasing at high  
 632 AOD, this would be consistent with a localised heating of the smoke layer.

634 Figure 14 also shows the September mean percentage of domain where  $TWP > 400 \text{ gm}^{-2}$  (named  
 635  $TWP_{400}$  in the plot) used to indicate the ‘convective nature’ of the season; higher values will be  
 636 associated with more numerous deep clouds throughout the domain hence a reasonable proxy for more  
 637 convection. Here we see strong relationships between AOD and convection, as well as the  $QV_{\text{column}}$  and  
 638  $NET_{\text{TOA}}$ . The regressions suggest that, on seasonal timescales, high-AOD years coincide with  
 639 suppressed convection, a drier atmosphere, and a net cooling radiative effect.



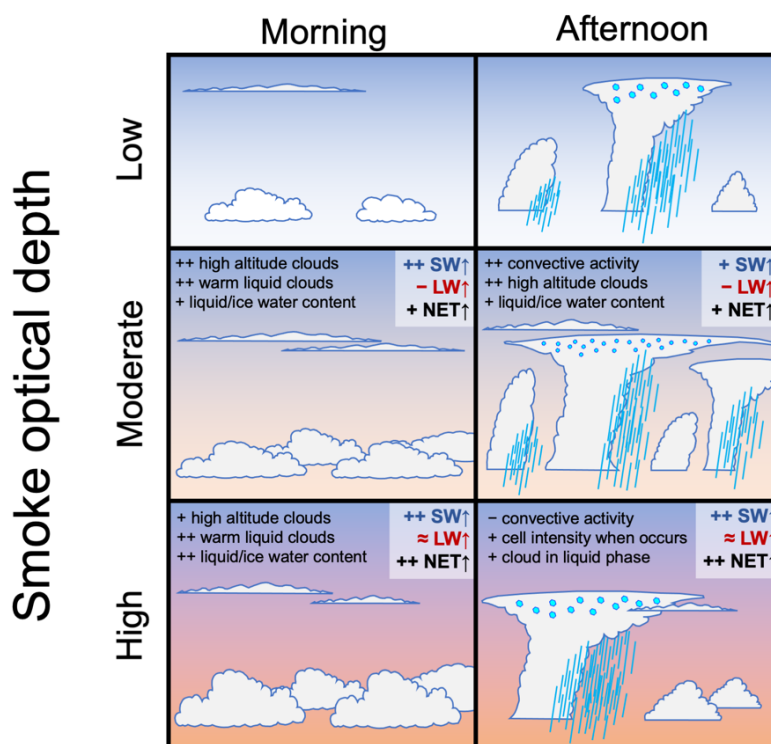
641  
 642 **Figure 14.** September mean AOD (left column),  $QV_{\text{column}}$  (center column), and  $NET_{\text{TOA}}$  (right column) from the  
 643 domain for each year as a function of the corresponding (from the top row downwards) percentage of domain  
 644 where  $TWP > 400 \text{ gm}^{-2}$ , August-September mean ENSO index, PDO index, and AMO index. The dotted line in  
 645 each plot shows the linear regression between the two datasets, with the corresponding R value shown at the top  
 646 of each plot.  $TWP_{400}$  is used as a metric to describe the ‘convective nature’ of the domain.

647



648 **4. Discussion and Conclusions**

649 In this study we used spatially and temporally collocated observations and estimates from multiple  
 650 satellite instruments and datasets to examine smoke-cloud-radiation interactions over the Amazon  
 651 rainforest during the month of September. We found evidence that smoke drives widespread changes  
 652 to the cloud field over the region consistent with ACI and ARI processes. **Figure 15** shows a schematic  
 653 summarising the main findings.  
 654



655 **Figure 15.** Summary of results from an 18-year timeseries of collocated MODIS, CERES, and AIRS observations  
 656 onboard TERRA (morning overpass) and AQUA (afternoon overpass) satellite platforms, combined with IMERG  
 657 precipitation estimates, during the peak biomass burning month of September over the Amazon rainforest. Panels  
 658 are shown for low (AOD < 0.1), moderate (AOD = 0.4), and high (AOD > 1.0) smoke optical depths. Annotations  
 659 are included to highlight primary responses to the cloud field and TOA outgoing radiation fluxes as compared to  
 660 the background low AOD scene; symbols depict increases (+), substantial increases (++) decreases (-), and  
 661 relatively little change (≈).  
 662

663 The Amazon atmosphere is very sensitive to low-to-moderate loadings of smoke where  $AOD \leq 0.4$ .  
 664 In the morning the smoke perturbation coincides with increases in the warm phase cloud coverage and  
 665 cloud optical thickness, consistent with a suppression of the warm rain process, whilst in the afternoon  
 666 there is a considerable enhancement in the formation and development of deep convection, enhancing  
 667 daily accumulated precipitation and intensity, and high-altitude cloud coverage. The high-altitude  
 668 clouds persist throughout the night and into the morning, possibly enhanced by smaller ice particle  
 669 sizes. The increased coverage and optical thickness of liquid clouds enhances the scene albedo, resulting  
 670 in a negative SW forcing; enhanced cirrus coverage partially offsets this via a decrease in LW, resulting  
 671 in a negative TOA net forcing.  
 672



673 At higher loadings of smoke where  $AOD > 0.4$  the liquid cloud coverage in the morning remains  
674 relatively stable with small increases in the cloud optical depth resulting in enhanced TOA cooling; an  
675 overall drying and warming of the boundary layer may play a role in limiting the cloud coverage extent.  
676 A primary response of the atmosphere in the afternoon is an overall suppression of convection,  
677 consistent with a stabilization of the atmosphere via surface cooling and elevated heating by ARI  
678 processes (Herbert et al., 2021). A reduction in cumulative precipitation and cirrus cloud coverage is  
679 consistent with the suppressed convection, along with a shift from the ice phase to liquid phase as mean  
680 cloud vertical extent decreases. At very high AOD accumulated precipitation remains comparable with  
681 background (very low AOD) scenes, despite weaker convection across the domain, which may suggest  
682 fewer, more intense, convective cells, consistent with the simulations of Herbert et al. (2021) and  
683 observations of delayed and more intense precipitation (Andreae et al., 2004; Gonçalves et al., 2015)  
684 though this would require further investigation to confirm.

685

686 These results are generally consistent with previous studies but also help to fill in some important  
687 knowledge gaps. Previous studies have focused on MODIS-AQUA retrievals to study the response of  
688 warm liquid clouds to aerosol over the region. Koren et al. (2004) used retrievals from the dry season  
689 of 2002 and reported a pronounced decrease in cloud fraction as the smoke optical depth increased.  
690 Using a similar methodology Yu et al. (2007) analysed data for two consecutive years and found  
691 opposing correlations (negative in 2002; positive in 2003). Ten Hoeve et al. (2011), focusing on a  
692 smaller domain and over four years, reported a consistent increasing cloud fraction with AOD; the  
693 authors found that the collocated CWV of the scene strongly influenced the cloud fraction and proposed  
694 that this behaviour may explain the opposing correlations in Yu et al. (2007). In our study we do not  
695 subset for one cloud type, and instead consider all clouds, making a direct comparison difficult.  
696 However, comparing to  $CF_{liquid}$  in our study for the AQUA overpass, we observe a shift towards higher  
697 coverage as AOD increases (**Figure 8b** and **Figure 10e**) for all years in the timeseries (not shown),  
698 consistent with Ten Hoeve et al. (2011) but not with Koren et al. (2004) and Yu et al. (2007). The  
699 inconsistencies may be explained by the differing methodologies, in that the authors removed scenes  
700 with cloud fractions  $> 0.8$  whereas in our study we do not. Subsetting our data to remove scenes with  
701  $CF_{liquid}$  or  $CF_{total} > 0.8$  has considerable impact on our results, as it removes a lot of data from the higher  
702 AOD scenes (**Figure 8**), biasing the dataset towards lower cloud fractions. The result of subsetting our  
703 data is a negative  $CF_{liquid}$ -AOD relationship at higher AOD and a weaker TOA radiative effect though  
704 of the same sign. This suggests that results from previous studies may be biased towards lower cloud  
705 fractions. However, a caveat is that the primary reason for restricting high CF values is to reduce  
706 misclassification of clouds and aerosol (Koren et al., 2010b) so some caution must be applied to these  
707 conclusions until further work can corroborate these findings.

708

709 Our conclusions may additionally explain behaviour reported by Koren et al. (2008). In the study the  
710 authors examine the relationship between low cloud fraction and AOD in MODIS-AQUA data. At  
711 higher AOD the authors find that subsetting the data to increasingly lower cloud fractions results in an  
712 increasingly negative  $CF_{liquid}$ -AOD relationship, attributed to greater sensitivity of low cloud-fraction  
713 scenes to aerosol absorption. This behaviour was also seen in our data when we subset the data to  
714 remove high  $CF_{liquid}$  scenes, therefore the results from Koren et al. (2008) could be alternatively  
715 interpreted as a result of dampening the underlying pathway, which is a pronounced shift from low to  
716 high  $CF_{liquid}$  scenes as AOD increases and modifies the widespread convective nature of the region. It  
717 is also possible that both processes are simultaneously occurring and contributing to the overall response  
718 of the cloud field.

719

720 A key process influencing the diurnal cycle of cloud cover and vertical distribution is via the  
721 modification to convection in the afternoon, driven by ARI at high AOD and ACI and/or thermal  
722 buoyancy at low AOD. We observe increasingly suppressed convection and precipitation for  $AOD >$   
723  $0.4$  during the AQUA overpass; this is consistent with modelling studies that report ARI-driven



724 stabilization of the lower atmosphere (Herbert et al., 2021; Liu et al., 2020; Martins et al., 2009; Wu et  
725 al., 2011) and suppressed (or delayed) convection with similar impacts to precipitation. Field studies  
726 from the region have similarly reported suppressed or delayed peak precipitation rates (Andreae et al.,  
727 2004; Bevan et al., 2008; Camponogara et al., 2014; Gonçalves et al., 2015), and remote observations  
728 from Koren et al. (2008) show a tendency for shallower convective clouds (less vertical extent) under  
729 high aerosol loading. The invigoration of convection at  $AOD < 0.4$  in our observations suggests an  
730 important process that has considerable implications for the region. Koren et al. (2008) report an  
731 increase in cloud fraction and taller convective clouds at small AOD perturbations, and Ten Hoeve et  
732 al. (2011) reported similar behaviour with  $COT_{liquid}$ . This is consistent with ACI-induced warm phase  
733 invigoration in shallow convection and in the warm base of deep convective cells (Marinescu et al.,  
734 2021; Koren et al., 2014; Seiki and Nakajima, 2014; Igel and van den Heever, 2021; Dagan et al., 2020),  
735 or through anomalous thermal buoyancy due to the fire itself (Zhang et al., 2019). The reduction in  
736 cloud top  $RE_{ice}$  (Figure 7c and d) with AOD for high-IWP scenes suggests more cloud droplets are  
737 reaching the freezing level; this may due to ACI processes or enhanced aerosol activation through  
738 thermally-induced anomalous buoyancy, making attribution of the dominant mechanism difficult.

739  
740 The analysis suggests an important inflection point in the Amazonian atmosphere's response to  
741 aerosol at  $AOD \approx 0.4$ . This value represents close to 50% of the retrieved AOD values over the time  
742 period analysed (Figure 1c), suggesting that in the near-present climate enhanced convection is as likely  
743 as suppressed convection. Current trends and future projections suggest biomass burning frequency and  
744 scale will increase throughout the Amazon rainforest (Stocker et al., 2013; Boisier et al., 2015); this  
745 will increase the likelihood of deep convection being suppressed and overall result in reduced cumulative  
746 precipitation to the region and potentially act as a positive feedback to fire activity and AOD.  
747 Simultaneously, increases in AOD are correlated with an overall brightening of the scene albedo  
748 (Figure 10) and a warmer, drier, boundary layer (Figure 9). Together with reduced precipitation there  
749 may be important impacts to the Amazonian biosphere and ecosystem.

750  
751 The pronounced diurnal cycle in the response of the clouds to aerosol is consistent with high-  
752 resolution modelling studies from the Amazon (Herbert et al., 2021) and over Borneo (Hodzic and  
753 Duvel, 2018), a region similarly dominated by biomass burning aerosol. The same contrasting responses  
754 in LWP and IWP were found when analysing scenes independently (Figure 2 and Figure 7) and the  
755 domain as a whole (Figure S2), suggesting the signal is independent of scale. These strong repeatable  
756 signals point towards the possibility of using the amplitude of the diurnal cycle in key cloud properties  
757 as an important source of information for constraining global ARI and ACI effects on the climate. This  
758 could be applied to both earth-system models and observations, and work towards reducing the  
759 uncertainty in current forcing estimates (Forster et al., 2021), with the caveat that current earth-system  
760 models used to produce the forcing estimates do not fully capture these convective processes. This study  
761 highlights the need for explicit treatment of convection in climate models.

762  
763 Both overpasses suggest AOD drives an overall SW cooling at the TOA due to changes in cloud  
764 properties. This is at odds with the theoretical model proposed by (Koren et al., 2004) who estimated  
765 that cloud field adjustments due to smoke (cloud thinning) over the Amazon would counteract some of  
766 the cooling, which suggests that the widespread radiative impact of smoke aerosol over the Amazon  
767 rainforest is more important than previously thought. We also find important changes to high-altitude  
768 cloud coverage, likely from deep convective outflow, which impact the outgoing LW at the TOA.  
769 Unlike over the tropical oceans (Koren et al., 2010a), these are of secondary importance when compared  
770 to changes in SW, but will influence the daily mean radiative effect due to their dominating role during  
771 the night. This study would benefit from using geostationary satellite data from GOES to validate our  
772 findings and extend the analysis throughout the full diurnal cycle, but would require well validated  
773 aerosol retrievals which are currently unavailable.



## 774 **Author Contribution**

775 RH designed the study and acquired the datasets. RH wrote the necessary scripts and analysed the  
776 dataset. RH prepared the manuscript with contributions from PS.

## 777 **Competing Interests**

778 Some authors are members of the editorial board of journal ACP. The peer-review process was  
779 guided by an independent editor, and the authors have also no other competing interests to declare.

## 780 **Acknowledgements**

781 This research was supported by the European Research Council (ERC) project constRaining the  
782 EffeCts of Aerosols on Precipitation (RECAP) under the European Union's Horizon 2020 research and  
783 innovation program with grant agreement no. 724602 and from the European Union's Horizon 2020  
784 research and innovation program project Constrained aerosol forcing for improved climate projections  
785 (FORCeS) under grant agreement No 821205.

## 786 **Data Availability**

787 All satellite datasets used in this analysis are available online. MODIS datasets are available via the  
788 NASA Level-1 and Atmosphere Archive & Distribution System (LAADS) Distributed Active Archive  
789 Center (DAAC) at <https://adsweb.modaps.eosdis.nasa.gov/archive/allData/61/>. IMERG daily and  
790 instantaneous data are available via the NASA Goddard Earth Sciences Data and Information Services  
791 Center (GESDISC) at <https://gpm1.gesdisc.eosdis.nasa.gov/data/>. ERA5 reanalysis datasets from the  
792 European Centre for Medium-Range Weather Forecasts (ECWMF) are available via the Natural  
793 Environment Research Council (NERC) Centre for Environmental Data analysis (CEDA), accessed via  
794 <https://data.ceda.ac.uk/badc/ecmwf-era5/>. AIRS data is available via NASA's Earth Science Data  
795 Systems (ESDS) program at <https://www.earthdata.nasa.gov/>. AERONET data is available from  
796 <https://aeronet.gsfc.nasa.gov/>. CERES datasets are available at <https://ceres.larc.nasa.gov/>. HYSPLIT  
797 back trajectories were performed online at <https://www.ready.noaa.gov/HYSPLIT.php>. The ecRad  
798 offline radiative transfer model is available via github at <https://github.com/ecmwf-ifs/ecrad>. This work  
799 used the ARCHER2 UK National Supercomputing Service (<https://www.archer2.ac.uk>). The spatially  
800 and temporally collocated datasets (at one- and two-degree resolution) are available alongside the  
801 relevant scripts for reproducing all figures at <http://doi.org/10.5281/zenodo.7007220>.

## 802 **References**

- 803 Andreae, M. O., Rosenfeld, D., Artaxo, P., Costa, A. A., Frank, G. P., Longo, K. M., and Silva-Dias, M. A. F.:  
804 Smoking Rain Clouds over the Amazon, *Science*, 303, 1337–1342, <https://doi.org/10.1126/science.1092779>,  
805 2004.
- 806 Aragão, L. E. O. C., Anderson, L. O., Fonseca, M. G., Rosan, T. M., Vedovato, L. B., Wagner, F. H., Silva, C. V. J.,  
807 Silva Junior, C. H. L., Arai, E., Aguiar, A. P., Barlow, J., Berenguer, E., Deeter, M. N., Domingues, L. G., Gatti, L.,  
808 Gloor, M., Malhi, Y., Marengo, J. A., Miller, J. B., Phillips, O. L., and Saatchi, S.: 21st Century drought-related  
809 fires counteract the decline of Amazon deforestation carbon emissions, *Nat Commun*, 9, 536,  
810 <https://doi.org/10.1038/s41467-017-02771-y>, 2018.
- 811 Bevan, S. L., North, P. R. J., Grey, W. M. F., Los, S. O., and Plummer, S. E.: The impact of atmospheric aerosol  
812 from biomass burning on Amazon dry-season drought, in: European Space Agency, (Special Publication) ESA  
813 SP, <https://doi.org/10.1029/2008jd011112>, 2008.
- 814 Boisier, J. P., Ciais, P., Ducharne, A., and Guimberteau, M.: Projected strengthening of Amazonian dry season  
815 by constrained climate model simulations, *Nature Climate Change*, 5, 656–660,  
816 <https://doi.org/10.1038/nclimate2658>, 2015.



ACPD

Herbert and Stier

- 817 Bond, T. C., Doherty, S. J., Fahey, D. W., Forster, P. M., Bernsten, T., DeAngelo, B. J., Flanner, M. G., Ghan, S.,  
818 Kärcher, B., Koch, D., Kinne, S., Kondo, Y., Quinn, P. K., Sarofim, M. C., Schultz, M. G., Schulz, M.,  
819 Venkataraman, C., Zhang, H., Zhang, S., Bellouin, N., Guttikunda, S. K., Hopke, P. K., Jacobson, M. Z., Kaiser, J.  
820 W., Klimont, Z., Lohmann, U., Schwarz, J. P., Shindell, D., Storelvmo, T., Warren, S. G., and Zender, C. S.:  
821 Bounding the role of black carbon in the climate system: A scientific assessment, *Journal of Geophysical*  
822 *Research: Atmospheres*, 118, 5380–5552, <https://doi.org/10.1002/jgrd.50171>, 2013.
- 823 Boulton, C. A., Lenton, T. M., and Boers, N.: Pronounced loss of Amazon rainforest resilience since the early  
824 2000s, *Nat. Clim. Chang.*, 12, 271–278, <https://doi.org/10.1038/s41558-022-01287-8>, 2022.
- 825 Braga, R. C., Rosenfeld, D., Weigel, R., Jurkat, T., Andreae, M. O., Wendisch, M., Pöhlker, M. L., Klimach, T.,  
826 Pöschl, U., Pöhlker, C., Voigt, C., Mahnke, C., Borrmann, S., Albrecht, R. I., Molleker, S., Vila, D. A., Machado, L.  
827 A. T., and Artaxo, P.: Comparing parameterized versus measured microphysical properties of tropical  
828 convective cloud bases during the ACRIDICON–CHUVA campaign, *Atmospheric Chemistry and Physics*, 17,  
829 7365–7386, <https://doi.org/10.5194/acp-17-7365-2017>, 2017.
- 830 Camponogara, G., Silva Dias, M. A. F., and Carrió, G. G.: Relationship between Amazon biomass burning  
831 aerosols and rainfall over the La Plata Basin, *Atmospheric Chemistry and Physics*, 14, 4397–4407,  
832 <https://doi.org/10.5194/acp-14-4397-2014>, 2014.
- 833 Cesana, G. and Storelvmo, T.: Improving climate projections by understanding how cloud phase affects  
834 radiation, *Journal of Geophysical Research: Atmospheres*, 122, 4594–4599,  
835 <https://doi.org/10.1002/2017JD026927>, 2017.
- 836 Ciemer, C., Rehm, L., Kurths, J., Donner, R. V., Winkelmann, R., and Boers, N.: An early-warning indicator for  
837 Amazon droughts exclusively based on tropical Atlantic sea surface temperatures, *Environ. Res. Lett.*, 15,  
838 094087, <https://doi.org/10.1088/1748-9326/ab9c9f>, 2020.
- 839 Dagan, G., Stier, P., Christensen, M., Cioni, G., Klocke, D., and Seifert, A.: Atmospheric energy budget response  
840 to idealized aerosol perturbation in tropical cloud systems, *Atmospheric Chemistry and Physics*, 20, 4523–  
841 4544, <https://doi.org/10.5194/acp-20-4523-2020>, 2020.
- 842 Fan, J., Rosenfeld, D., Zhang, Y., Giangrande, S. E., Li, Z., Machado, L. A. T., Martin, S. T., Yang, Y., Wang, J.,  
843 Artaxo, P., Barbosa, H. M. J., Braga, R. C., Comstock, J. M., Feng, Z., Gao, W., Gomes, H. B., Mei, F., Pöhlker, C.,  
844 Pöhlker, M. L., Pöschl, U., and De Souza, R. A. F.: Substantial convection and precipitation enhancements by  
845 ultrafine aerosol particles, *Science*, 359, 411–418, <https://doi.org/10.1126/science.aan8461>, 2018.
- 846 Forster, P., Storelvmo, T., Armour, K., Collins, W., Dufresne, J.-L., Frame, D., Lunt, D., J., Mauritsen, T., Palmer,  
847 M., D., Watanabe, M., Wild, M., and Zhang, H.: The Earth's Energy Budget, Climate Feedbacks, and Climate  
848 Sensitivity, in: *Climate Change 2021: The Physical Science Basis. Contribution of Working Group I to the Sixth*  
849 *Assessment Report of the Intergovernmental Panel on Climate Change*, Cambridge University Press,  
850 Cambridge, United Kingdom and New York, NY, USA, 923–1054, <https://doi.org/10.1017/9781009157896.009>,  
851 2021.
- 852 Gonçalves, W. A., Machado, L. A. T., and Kirstetter, P.-E.: Influence of biomass aerosol on precipitation over the  
853 Central Amazon: an observational study, *Atmospheric Chemistry and Physics*, 15, 6789–6800,  
854 <https://doi.org/10.5194/acp-15-6789-2015>, 2015.
- 855 Gonzalez-Alonso, L., Val Martin, M., and Kahn, R. A.: Biomass-burning smoke heights over the Amazon  
856 observed from space, *Atmospheric Chemistry and Physics*, 19, 1685–1702, <https://doi.org/10.5194/acp-19-1685-2019>, 2019.
- 858 Gryspeerdt, E., Stier, P., White, B. A., and Kipling, Z.: Wet scavenging limits the detection of aerosol effects on  
859 precipitation, *Atmospheric Chemistry and Physics*, 15, 7557–7570, <https://doi.org/10.5194/acp-15-7557-2015>,  
860 2015.



ACPD

Herbert and Stier

- 861 Herbert, R., Stier, P., and Dagan, G.: Isolating Large-Scale Smoke Impacts on Cloud and Precipitation Processes  
862 Over the Amazon With Convection Permitting Resolution, *Journal of Geophysical Research: Atmospheres*, 126,  
863 e2021JD034615, <https://doi.org/10.1029/2021JD034615>, 2021.
- 864 Herbert, R. J., Bellouin, N., Highwood, E. J., and Hill, A. A.: Diurnal cycle of the semi-direct effect from a  
865 persistent absorbing aerosol layer over marine stratocumulus in large-eddy simulations, *Atmospheric*  
866 *Chemistry and Physics*, 20, 1317–1340, <https://doi.org/10.5194/acp-20-1317-2020>, 2020.
- 867 Hodzic, A. and Duvel, J. P.: Impact of Biomass Burning Aerosols on the Diurnal Cycle of Convective Clouds and  
868 Precipitation Over a Tropical Island, *Journal of Geophysical Research: Atmospheres*, 123, 1017–1036,  
869 <https://doi.org/10.1002/2017JD027521>, 2018.
- 870 Hogan, R. J. and Bozzo, A.: A Flexible and Efficient Radiation Scheme for the ECMWF Model, *Journal of*  
871 *Advances in Modeling Earth Systems*, 10, 1990–2008, <https://doi.org/10.1029/2018MS001364>, 2018.
- 872 Holanda, B. A., Pöhlker, M. L., Walter, D., Saturno, J., Sörgel, M., Ditas, J., Ditas, F., Schulz, C., Aurélio Franco,  
873 M., Wang, Q., Donth, T., Artaxo, P., Barbosa, H. M. J., Borrmann, S., Braga, R., Brito, J., Cheng, Y., Dollner, M.,  
874 Kaiser, J. W., Klimach, T., Knote, C., Krüger, O. O., Fütterer, D., Lavric, J. t.V., Ma, N., MacHado, L. A. T., Ming, J.,  
875 Morais, F. G., Paulsen, H., Sauer, D., Schlager, H., Schneider, J., Su, H., Weinzierl, B., Walser, A., Wendisch, M.,  
876 Ziereis, H., Zöger, M., Pöschl, U., Andreae, M. O., and Pöhlker, C.: Influx of African biomass burning aerosol  
877 during the Amazonian dry season through layered transatlantic transport of black carbon-rich smoke,  
878 *Atmospheric Chemistry and Physics*, 20, 4757–4785, <https://doi.org/10.5194/acp-20-4757-2020>, 2020.
- 879 Igel, A. L. and van den Heever, S. C.: Invigoration or Elevation of Convective Clouds by Aerosols?, *Geophysical*  
880 *Research Letters*, 48, e2021GL093804, <https://doi.org/10.1029/2021GL093804>, 2021.
- 881 Jimenez, J. C., Marengo, J. A., Alves, L. M., Sulca, J. C., Takahashi, K., Ferrett, S., and Collins, M.: The role of  
882 ENSO flavours and TNA on recent droughts over Amazon forests and the Northeast Brazil region, *International*  
883 *Journal of Climatology*, 41, 3761–3780, <https://doi.org/10.1002/joc.6453>, 2021.
- 884 Jiménez-Muñoz, J. C., Mattar, C., Barichivich, J., Santamaría-Artigas, A., Takahashi, K., Malhi, Y., Sobrino, J. A.,  
885 and Schrier, G. van der: Record-breaking warming and extreme drought in the Amazon rainforest during the  
886 course of El Niño 2015–2016, *Sci Rep*, 6, 33130, <https://doi.org/10.1038/srep33130>, 2016.
- 887 Khain, A., Rosenfeld, D., and Pokrovsky, A.: Aerosol impact on the dynamics and microphysics of deep  
888 convective clouds, *Quarterly Journal of the Royal Meteorological Society*, 131, 2639–2663,  
889 <https://doi.org/10.1256/qj.04.62>, 2005.
- 890 Koch, D. and Del Genio, A. D.: Black carbon semi-direct effects on cloud cover: review and synthesis,  
891 *Atmospheric Chemistry and Physics*, 10, 7685–7696, <https://doi.org/10.5194/acp-10-7685-2010>, 2010.
- 892 Koren, I., Kaufman, Y. J., Remer, L. A., and Martins, J. V.: Measurement of the Effect of Amazon Smoke on  
893 Inhibition of Cloud Formation, *Science*, 303, 1342–1345, <https://doi.org/10.1126/science.1089424>, 2004.
- 894 Koren, I., Vanderlei Martins, J., Remer, L. A., and Afargan, H.: Smoke invigoration versus inhibition of clouds  
895 over the amazon, *Science*, 321, 946–949, <https://doi.org/10.1126/science.1159185>, 2008.
- 896 Koren, I., Remer, L. A., Altaratz, O., Martins, J. V., and Davidi, A.: Aerosol-induced changes of convective cloud  
897 anvils produce strong climate warming, *Atmos. Chem. Phys.*, 10, 5001–5010, <https://doi.org/10.5194/acp-10-5001-2010>, 2010a.
- 899 Koren, I., Feingold, G., and Remer, L. A.: The invigoration of deep convective clouds over the Atlantic: aerosol  
900 effect, meteorology or retrieval artifact?, *Atmos. Chem. Phys.*, 10, 8855–8872, <https://doi.org/10.5194/acp-10-8855-2010>, 2010b.
- 902 Koren, I., Dagan, G., and Altaratz, O.: From aerosol-limited to invigoration of warm convective clouds, *Science*,  
903 344, 1143–1146, <https://doi.org/10.1126/science.1252595>, 2014.



- 904 Lebo, Z.: A numerical investigation of the potential effects of aerosol-induced warming and updraft width and  
905 slope on updraft intensity in deep convective clouds, *Journal of the Atmospheric Sciences*, 75, 535–554,  
906 <https://doi.org/10.1175/JAS-D-16-0368.1>, 2018.
- 907 Lee, S. S., Feingold, G., McComiskey, A., Yamaguchi, T., Koren, I., Vanderlei Martins, J., and Yu, H.: Effect of  
908 gradients in biomass burning aerosol on shallow cumulus convective circulations, *Journal of Geophysical*  
909 *Research: Atmospheres*, 119, 9948–9964, <https://doi.org/10.1002/2014JD021819>, 2014.
- 910 Libonati, R., Pereira, J. M. C., Da Camara, C. C., Peres, L. F., Oom, D., Rodrigues, J. A., Santos, F. L. M., Trigo, R.  
911 M., Gouveia, C. M. P., Machado-Silva, F., Enrich-Prast, A., and Silva, J. M. N.: Twenty-first century droughts  
912 have not increasingly exacerbated fire season severity in the Brazilian Amazon, *Sci Rep*, 11, 4400,  
913 <https://doi.org/10.1038/s41598-021-82158-8>, 2021.
- 914 Liu, L., Cheng, Y., Wang, S., Wei, C., Pöhlker, M., Pöhlker, C., Artaxo, P., Shrivastava, M., Andreae, M., Pöschl,  
915 U., and Su, H.: Impact of biomass burning aerosols on radiation, clouds, and precipitation over the Amazon  
916 during the dry season: dependence of aerosol-cloud and aerosol-radiation interactions on aerosol loading,  
917 *Atmospheric Chemistry and Physics*, 1–50, <https://doi.org/10.5194/acp-2020-191>, 2020.
- 918 Liu, S., Aiken, A. C., Arata, C., Dubey, M. K., Stockwell, C. E., Yokelson, R. J., Stone, E. A., Jayarathne, T.,  
919 Robinson, A. L., DeMott, P. J., and Kreidenweis, S. M.: Aerosol single scattering albedo dependence on biomass  
920 combustion efficiency: Laboratory and field studies, *Geophysical Research Letters*, 41, 742–748,  
921 <https://doi.org/10.1002/2013GL058392>, 2014.
- 922 Marinescu, P. J., Heever, S. C. van den, Heikenfeld, M., Barrett, A. I., Barthlott, C., Hoose, C., Fan, J., Fridlind, A.  
923 M., Matsui, T., Miltenberger, A. K., Stier, P., Vie, B., White, B. A., and Zhang, Y.: Impacts of Varying  
924 Concentrations of Cloud Condensation Nuclei on Deep Convective Cloud Updrafts—A Multimodel Assessment,  
925 *Journal of the Atmospheric Sciences*, 78, 1147–1172, <https://doi.org/10.1175/JAS-D-20-0200.1>, 2021.
- 926 Martins, J. A. and Silva Dias, M. A. F.: The impact of smoke from forest fires on the spectral dispersion of cloud  
927 droplet size distributions in the Amazonian region, *Environ. Res. Lett.*, 4, 015002,  
928 <https://doi.org/10.1088/1748-9326/4/1/015002>, 2009.
- 929 Martins, J. A., Silva Dias, M. A. F., and Gonçalves, F. L. T.: Impact of biomass burning aerosols on precipitation  
930 in the Amazon: A modeling case study, *Journal of Geophysical Research*, 114,  
931 <https://doi.org/10.1029/2007jd009587>, 2009.
- 932 McClure, C. D., Lim, C. Y., Hagan, D. H., Kroll, J. H., and Cappa, C. D.: Biomass-burning-derived particles from a  
933 wide variety of fuels – Part 1: Properties of primary particles, *Atmospheric Chemistry and Physics*, 20, 1531–  
934 1547, <https://doi.org/10.5194/acp-20-1531-2020>, 2020.
- 935 de Oliveira, G., Chen, J. M., Mataveli, G. A. V., Chaves, M. E. D., Seixas, H. T., da Cardozo, F. S., Shimabukuro, Y.  
936 E., He, L., Stark, S. C., and dos Santos, C. A. C.: Rapid recent deforestation incursion in a vulnerable indigenous  
937 land in the Brazilian Amazon and fire-driven emissions of fine particulate aerosol pollutants, *Forests*, 11, 829–  
938 829, <https://doi.org/10.3390/f11080829>, 2020.
- 939 Palácios, R. da S., Romera, K. S., Curado, L. F. A., Banga, N. M., Rothmund, L. D., Sallo, F. da S., Morais, D.,  
940 Santos, A. C. A., Moraes, T. J., Morais, F. G., Landulfo, E., Franco, M. A. de M., Kuhnen, I. A., Marques, J. B.,  
941 Nogueira, J. de S., Júnior, L. C. G. do V., and Rodrigues, T. R.: Long Term Analysis of Optical and Radiative  
942 Properties of Aerosols in the Amazon Basin, *Aerosol Air Qual. Res.*, 20, 139–154,  
943 <https://doi.org/10.4209/aaqr.2019.04.0189>, 2020.
- 944 Petters, M. D., Carrico, C. M., Kreidenweis, S. M., Prenni, A. J., DeMott, P. J., Collett Jr., J. L., and Moosmüller,  
945 H.: Cloud condensation nucleation activity of biomass burning aerosol, *Journal of Geophysical Research:*  
946 *Atmospheres*, 114, <https://doi.org/10.1029/2009JD012353>, 2009.
- 947 Rosário, N. E., Yamasoe, M. A., Brindley, H., Eck, T. F., and Schafer, J.: Downwelling solar irradiance in the  
948 biomass burning region of the southern Amazon: Dependence on aerosol intensive optical properties and role



ACPD

Herbert and Stier

- 949 of water vapor, *Journal of Geophysical Research: Atmospheres*, 116, <https://doi.org/10.1029/2011JD015956>,  
950 2011.
- 951 Sayer, A. M., Hsu, N. C., Lee, J., Kim, W. V., and Dutcher, S. T.: Validation, Stability, and Consistency of MODIS  
952 Collection 6.1 and VIIRS Version 1 Deep Blue Aerosol Data Over Land, *Journal of Geophysical Research:*  
953 *Atmospheres*, 124, 4658–4688, <https://doi.org/10.1029/2018JD029598>, 2019.
- 954 Seiki, T. and Nakajima, T.: Aerosol Effects of the Condensation Process on a Convective Cloud Simulation,  
955 *Journal of the Atmospheric Sciences*, 71, 833–853, <https://doi.org/10.1175/JAS-D-12-0195.1>, 2014.
- 956 Stein, A. F., Draxler, R. R., Rolph, G. D., Stunder, B. J. B., Cohen, M. D., and Ngan, F.: NOAA's HYSPLIT  
957 Atmospheric Transport and Dispersion Modeling System, *Bulletin of the American Meteorological Society*, 96,  
958 2059–2077, <https://doi.org/10.1175/BAMS-D-14-00110.1>, 2015.
- 959 Stocker, T. F., Qin, D., Plattner, G.-K., Tignor, M., Allen, S. K., Boschung, J., Nauels, A., Xia, Y., Bex, V., and  
960 Midgley, P. M.: *AR5 Climate Change 2013: The Physical Science Basis — IPCC*, Cambridge University Press,  
961 Cambridge, United Kingdom and New York, 1585–1585, 2013.
- 962 Ten Hoeve, J. E., Remer, L. A., and Jacobson, M. Z.: Microphysical and radiative effects of aerosols on warm  
963 clouds during the Amazon biomass burning season as observed by MODIS: impacts of water vapor and land  
964 cover, *Atmospheric Chemistry and Physics*, 11, 3021–3036, <https://doi.org/10.5194/acp-11-3021-2011>, 2011.
- 965 Thornhill, G. D., Ryder, C. L., Highwood, E. J., Shaffrey, L. C., and Johnson, B. T.: The effect of South American  
966 biomass burning aerosol emissions on the regional climate, *Atmospheric Chemistry and Physics*, 18, 5321–  
967 5342, <https://doi.org/10.5194/acp-18-5321-2018>, 2018.
- 968 Twohy, C. H., Toohey, D. W., Levin, E. J. T., DeMott, P. J., Rainwater, B., Garofalo, L. A., Pothier, M. A., Farmer,  
969 D. K., Kreidenweis, S. M., Pöhrl, R. P., Murphy, S. M., Reeves, J. M., Moore, K. A., and Fischer, E. V.: Biomass  
970 Burning Smoke and Its Influence on Clouds Over the Western U. S., *Geophysical Research Letters*, 48,  
971 e2021GL094224, <https://doi.org/10.1029/2021GL094224>, 2021.
- 972 Vakkari, V., Kerminen, V.-M., Beukes, J. P., Tiitta, P., van Zyl, P. G., Josipovic, M., Venter, A. D., Jaars, K.,  
973 Worsnop, D. R., Kulmala, M., and Laakso, L.: Rapid changes in biomass burning aerosols by atmospheric  
974 oxidation, *Geophysical Research Letters*, 41, 2644–2651, <https://doi.org/10.1002/2014GL059396>, 2014.
- 975 Wei, J., Li, Z., Peng, Y., and Sun, L.: MODIS Collection 6.1 aerosol optical depth products over land and ocean:  
976 validation and comparison, *Atmospheric Environment*, 201, 428–440,  
977 <https://doi.org/10.1016/j.atmosenv.2018.12.004>, 2019.
- 978 Wendisch, M., Poschl, U., Andreae, M. O., MacHado, L. A. T., Albrecht, R., Schlager, H., Rosenfeld, D., Martin, S.  
979 T., Abdelmonem, A., Afchine, A., Araujo, A. C., Artaxo, P., Aufmhoff, H., Barbosa, H. M. J., Borrmann, S., Braga,  
980 R., Buchholz, B., Cecchini, M. A., Costa, A., Curtius, J., Dollner, M., Dorf, M., Dreiling, V., Ebert, V., Ehrlich, A.,  
981 Ewald, F., Fisch, G., Fix, A., Frank, F., Futterer, D., Heckl, C., Heidelberg, F., Huneke, T., Jakel, E., Jarvinen, E.,  
982 Jurkat, T., Kanter, S., Kastner, U., Kenntner, M., Kesselmeier, J., Klimach, T., Knecht, M., Kohl, R., Kolling, T.,  
983 Kramer, M., Kruger, M., Krisna, T. C., Lavric, J. V., Longo, K., Mahnke, C., Manzi, A. O., Mayer, B., Mertes, S.,  
984 Minikin, A., Molleker, S., Munch, S., Nillius, B., Pfeilsticker, K., Pohlker, C., Roiger, A., Rose, D., Rosenow, D.,  
985 Sauer, D., Schnaiter, M., Schneider, J., Schulz, C., De Souza, R. A. F., Spanu, A., Stock, P., Vila, D., Voigt, C.,  
986 Walsler, A., Walter, D., Weigel, R., Weinzierl, B., Werner, F., Yamasoe, M. A., Ziereis, H., Zinner, T., and Zoger,  
987 M.: Acridicon-chuva campaign: Studying tropical deep convective clouds and precipitation over amazonia using  
988 the New German research aircraft HALO, *Bulletin of the American Meteorological Society*, 97, 1885–1908,  
989 <https://doi.org/10.1175/BAMS-D-14-00255.1>, 2016.
- 990 van der Werf, G. R., Randerson, J. T., Giglio, L., van Leeuwen, T. T., Chen, Y., Rogers, B. M., Mu, M., van Marle,  
991 M. J. E., Morton, D. C., Collatz, G. J., Yokelson, R. J., and Kasibhatla, P. S.: Global fire emissions estimates during  
992 1997–2016, *Earth System Science Data*, 9, 697–720, <https://doi.org/10.5194/essd-9-697-2017>, 2017.



ACPD

Herbert and Stier

- 993 White, B., Gryspeerdt, E., Stier, P., Morrison, H., Thompson, G., and Kipling, Z.: Uncertainty from the choice of  
994 microphysics scheme in convection-permitting models significantly exceeds aerosol effects, *Atmospheric*  
995 *Chemistry and Physics*, 17, 12145–12175, <https://doi.org/10.5194/acp-17-12145-2017>, 2017.
- 996 Wu, L., Su, H., and Jiang, J. H.: Regional simulations of deep convection and biomass burning over South  
997 America: 2. Biomass burning aerosol effects on clouds and precipitation, *Journal of Geophysical Research*  
998 *Atmospheres*, 116, <https://doi.org/10.1029/2011JD016106>, 2011.
- 999 Yoon, J.-H. and Zeng, N.: An Atlantic influence on Amazon rainfall, *Clim Dyn*, 34, 249–264,  
1000 <https://doi.org/10.1007/s00382-009-0551-6>, 2010.
- 1001 Yu, H., Fu, R., Dickinson, R. E., Zhang, Y., Chen, M., and Wang, H.: Interannual variability of smoke and warm  
1002 cloud relationships in the Amazon as inferred from MODIS retrievals, *Remote Sensing of Environment*, 111,  
1003 435–449, <https://doi.org/10.1016/j.rse.2007.04.003>, 2007.
- 1004 Zaveri, R. A., Wang, J., Fan, J., Zhang, Y., Shilling, J. E., Zelenyuk, A., Mei, F., Newsom, R., Pekour, M., Tomlinson,  
1005 J., Comstock, J. M., Shrivastava, M., Fortner, E., Machado, L. A. T., Artaxo, P., and Martin, S. T.: Rapid growth of  
1006 anthropogenic organic nanoparticles greatly alters cloud life cycle in the Amazon rainforest, *Science Advances*,  
1007 8, eabj0329, <https://doi.org/10.1126/sciadv.abj0329>, 2022.
- 1008 Zhang, R., Khalizov, A. F., Pagels, J., Zhang, D., Xue, H., and McMurry, P. H.: Variability in morphology,  
1009 hygroscopicity, and optical properties of soot aerosols during atmospheric processing, *Proceedings of the*  
1010 *National Academy of Sciences*, 105, 10291–10296, <https://doi.org/10.1073/pnas.0804860105>, 2008a.
- 1011 Zhang, Y., Fu, R., Yu, H., Dickinson, R. E., Juarez, R. N., Chin, M., and Wang, H.: A regional climate model study  
1012 of how biomass burning aerosol impacts land-atmosphere interactions over the Amazon, *Journal of*  
1013 *Geophysical Research*, 113, <https://doi.org/10.1029/2007jd009449>, 2008b.
- 1014 Zhang, Y., Fu, R., Yu, H., Qian, Y., Dickinson, R., Silva Dias, M. A. F., da Silva Dias, P. L., and Fernandes, K.: Impact  
1015 of biomass burning aerosol on the monsoon circulation transition over Amazonia, *Geophysical Research*  
1016 *Letters*, 36, L10814–L10814, <https://doi.org/10.1029/2009GL037180>, 2009.
- 1017 Zhang, Y., Fan, J., Logan, T., Li, Z., and Homeyer, C. R.: Wildfire Impact on Environmental Thermodynamics and  
1018 Severe Convective Storms, *Geophysical Research Letters*, 46, 10082–10093,  
1019 <https://doi.org/10.1029/2019GL084534>, 2019.
- 1020 Zhao, B., Wang, Y., Gu, Y., Liou, K.-N., Jiang, J. H., Fan, J., Liu, X., Huang, L., and Yung, Y. L.: Ice nucleation by  
1021 aerosols from anthropogenic pollution, *Nat. Geosci.*, 12, 602–607, [https://doi.org/10.1038/s41561-019-0389-](https://doi.org/10.1038/s41561-019-0389-4)  
1022 4, 2019.
- 1023  
1024